



BRNO UNIVERSITY OF TECHNOLOGY
VYSOKÉ UČENÍ TECHNICKÉ V BRNĚ



FACULTY OF MECHANICAL ENGINEERING
INSTITUTE OF PHYSICAL ENGINEERING

FAKULTA STROJNÍHO INŽENÝRSTVÍ
ÚSTAV FYZIKÁLNÍHO INŽENÝRSTVÍ

PREPARATION AND CHARACTERISATION OF ELECTRICAL PROPERTIES OF GRAPHENE CVD SINGLE CRYSTALS

PŘÍPRAVA A CHARAKTERIZACE ELEKTRICKÝCH VLASTNOSTÍ CVD
GRAFENOVÝCH MONOKRYSTALŮ

MASTER'S THESIS
DIPLOMOVÁ PRÁCE

AUTHOR
AUTOR PRÁCE

Bc. JAN HULVA

SUPERVISOR
VEDOUCÍ PRÁCE

Ing. JINDŘICH MACH, Ph.D.

BRNO 2014

Vysoké učení technické v Brně, Fakulta strojního inženýrství

Ústav fyzikálního inženýrství

Akademický rok: 2013/2014

ZADÁNÍ DIPLOMOVÉ PRÁCE

student(ka): Bc. Jan Hulva

který/která studuje v **magisterském navazujícím studijním programu**

obor: **Fyzikální inženýrství a nanotechnologie (3901T043)**

editel ústavu Vám v souladu se zákonem 111/1998 o vysokých školách a se Studijním a zkušebním řádem VUT v Brně určuje následující téma diplomové práce:

Příprava a charakterizace elektrických vlastností CVD grafenových monokrystal

v anglickém jazyce:

The preparation and characterisation of electrical properties of graphene CVD monocrystals

Stručná charakteristika problematiky úkolu:

Úkolem diplomové práce bude provedení rešeršní studie přípravy grafenových monokrystalů. Student provede sérii depozic grafenových monokrystalů za různých fyzikálních podmínek (tlak, tok, substrát, ...). Připravené monokrystaly budou čištěny a přeneseny na vhodný substrát. Dále budou provedena měření za účelem charakterizace elektrických vlastností těchto monokrystalů. Takto vyhotovené grafenové monokrystaly budou analyzovány metodami PPMS, XPS, AFM, SEM a Ramanovy spektroskopie.

Cíle diplomové práce:

- 1) Provedení rešeršní studie přípravy monokrystalů grafenu.
- 2) Příprava monokrystalů grafenu.
- 3) Provedení vhodného kontaktování monokrystalů grafenu.
- 4) Charakterizace povrchových a elektrických vlastností grafenových monokrystalů.

Seznam odborné literatury:

- [1] Mehdipour H., Ostrikov K., Kinetics of Low-Pressure , Single-Crystalline Structure, (11), 10276–10286 (2012).
- [2] Li Q., Chou H., Zhong J. H., Liu J.Y., Dolocan A., Zhang J., Zhou Y., et al., Growth of adlayer graphene on Cu studied by carbon isotope-labeling. Nano letters, (2013).

Vedoucí diplomové práce: Ing. Jindřich Mach, Ph.D.

Termín odevzdání diplomové práce je stanoven časovým plánem akademického roku 2013/2014.

V Brně, dne 23.10.2013

L.S.

prof. RNDr. Tomáš Šikola, CSc.
editel ústavu

prof. RNDr. Miroslav Doupovec, CSc., dr. h. c.
Děkan fakulty

ABSTRACT

Chemical Vapor Deposition (CVD) of graphene is a method for graphene synthesis capable of producing predominantly single layer graphene of large areas. A part of the experimental work in this thesis is focused on the deposition and analysis of single-crystalline graphene domains grown by CVD on a copper foil. These domains are analyzed by the optical microscopy, scanning electron microscopy, atomic force microscopy and Raman spectroscopy. The next part of the work is devoted to identification of defects found on the Cu foil after the deposition of graphene by means of energy dispersive X-ray spectroscopy. The number of the defects was reduced significantly by an adjustment of the deposition system, although some of them remained. The measurements on electronic transport properties of deposited graphene layers were performed on polycrystalline layers. The results contain measurements of graphene in vacuum with applied back gate voltage and at low temperature with applied magnetic field.

KEYWORDS

graphene, chemical vapor deposition, copper substrate, electronic transport properties

ABSTRAKT

Chemická depozice grafenu z plynné fáze (CVD) je metoda schopná produkovat grafenové monovrstvy velkých rozměrů. Část experimentů v rámci této diplomové práce je zaměřena na depozici a analýzu grafenových monokrystalů připravených metodou CVD na měděném substrátu. Pro analýzu grafenových domén je použito optické mikroskopie, elektronové mikroskopie, mikroskopie atomárních sil a Ramanovy spektroskopie. Úkolem další části je studium defektů pozorovaných na mědi po depozici grafenu pomocí energiově disperzní rentgenové spektroskopie. Přestože úprava depozičního systému vedla ke snížení počtu defektů, jejich úplného odstranění se nepodařilo dosáhnout. Elektro-transportní měření byla provedena na polykrystalických vrstvách grafenu. Výsledky této části zahrnují měření ve vakuu s přiloženým hradlovým napětím, jakož i měření při nízkých teplotách v magnetickém poli.

KLÍČOVÁ SLOVA

grafen, chemická depozice z plynné fáze, měděný substrát, elektro-transportní vlastnosti

HULVA, J.: *Příprava a charakterizace elektrických vlastností CVD grafenových monokrystalů*. Brno: Vysoké učení technické v Brně, Fakulta strojního inženýrství, 2014. 53 s. Vedoucí práce Ing. Jindřich Mach, Ph.D.

Prohlašuji, že jsem tuto diplomovou práci vypracoval samostatně, pouze za odborného vedení Ing. Jindřich Macha, Ph.D., a že veškeré podklady, ze kterých jsem čerpal, jsou uvedeny v seznamu použité literatury.

Bc. Jan Hulva

Děkuji svému vedoucím Ing. Jindřichu Machovi, Ph.D. za odborné vedení v průběhu vypracování této práce. Dále děkuji Ing. Miroslavu Bartošíkovi, Ph.D., Ing. Zuzaně Liškové, Ing. Pavlu Procházce, Ing. Martinu Konečnému a celému kolektivu grafenové skupiny za cenné konzultace a podnětnou spolupráci.

Contents

1	Introduction	1
2	Graphene Properties	2
2.1	Structure and electronic properties	3
2.2	Quantum Hall effect in graphene	7
2.3	Raman spectra of graphene	8
3	Graphene Preparation Methods	11
3.1	Chemical vapor deposition	12
3.1.1	Types of Cu substrates	15
3.1.2	Role of the crystallographic orientation of the substrate . . .	16
3.1.3	Role of substrate roughness and surface impurities	16
3.1.4	Role of the deposition temperature	18
3.1.5	Role of the deposition pressure and reaction gases partial pressures	18
3.1.6	CVD Modifications	20
3.1.7	Graphene Transfer	20
4	Experimental setup and methods description	22
4.1	Chemical Vapor Deposition system and transfer technology	22
4.1.1	Deposition system	22
4.1.2	Graphene Transfer and Contacting	23
4.2	Scanning Electron Microscopy	25
4.2.1	Energy Dispersive X-ray spectroscopy	25
4.2.2	Electron Beam Lithography	26
4.3	Raman Spectroscopy	26
4.4	Optical Microscopy	27
4.5	Atomic Force Microscopy	27
4.6	Electronic transport measurement	27
4.6.1	Electronic transport measurement in vacuum	28
4.6.1.1	Measurement of back-gate leakage current	29
4.6.2	Low Temperature Measurement Setup	29
5	Experimental Results	31

5.1	Graphene Single Crystals	31
5.1.1	Graphene single crystals on Cu foils	31
5.1.2	Graphene single-crystals on SiO ₂ /Si	34
5.2	Polycrystalline graphene and study of impurities	35
5.3	Electronic transport measurement	39
5.3.1	Vacuum measurement of polycrystalline graphene	39
5.3.2	Low Temperature and Magnetic field Measurement	44
6	Conclusion	46
	Bibliography	48

Chapter 1

Introduction

Since the first experimental demonstration of its electronic transport properties in 2004 [1], graphene has received considerable attention by broader scientific community. Since that time, this one-atom thick layer of carbon atoms has been intensively studied by many research groups for its unique properties which have led to numerous predictions of high impact of graphene on various commercial applications in the near future [2]. Consequently, the work by Geim and Novoselov resulting into the graphene discovery was awarded by the Nobel Prize in Physics in 2010 for “groundbreaking experiments regarding the two-dimensional material graphene” [3].

There are several graphene properties attracting interests of many scientists and engineers from different research fields. The exceptionally high charge carrier mobility is promising for a development of graphene-based high-frequency transistors [4]. Graphene is considered as a possible replacement for indium tin oxide as a flexible electrode in OLED devices and solar cells for its optical transparency and electric conductivity [5, 6]. In combination with its elasticity, graphene can be a part of the next generation flexible electronics [7]. Another examples of graphene potential are the gas molecules sensing [8], graphene composite materials [9, 10], bio-applications [11, 12] and many others. Even though the range of possible applications is really wide, graphene technology is relatively young and there are several problems to be solved before graphene commercial utilization.

One of the important challenges of graphene is its production. There are several methods of graphene fabrication which differ in quality of the final product and only some of these methods are suitable for the mass production. The subject of this thesis is the Chemical Vapor Deposition (CVD) of graphene. This method provides a relatively simple way for graphene synthesis and has shown capability of producing large-area graphene for industrial applications [13].

This thesis is focused on synthesis of graphene by CVD on copper substrates and characterization of graphene structures by various methods. Chapter 2 and 3 are the review parts of the thesis. Chapter 2 describes graphene in general and discusses general and electronic transport properties of graphene. Chapter 3 reviews the CVD process of graphene synthesis including the graphene growth on metal catalysts, transfer onto insulating substrates and contacting of graphene structures. Chapters 4 and 5 present the obtained experimental results from CVD deposition of graphene and electronic transport measurements, respectively.

Chapter 2

Graphene Properties

Carbon (C) is one of the most abundant element in the universe. Its ability to form long chains of C-C bonds, to combine them with hydrogen and other elements and to form complex molecules make carbon the cornerstone of the organic chemistry.

In addition to the ground state of unbound atom, carbon can also exist in hybridized states (Figure 2.1). In the sp^3 state, electrons in hybridized orbital can participate in four σ (single) bonds. In the sp^2 hybridization, only three electrons in hybridized orbital are available for forming σ bonds and electron from p orbital can form a π bond. The sp hybridization is characteristic for a carbon atom involved in a triple bond.







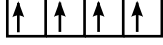




${}^6\text{C}$	sp	sp^2	sp^3
2p 	$p_{y,z}$ 	p_z 	
2s 	sp 	sp^2 	sp^3 
1s 	1s 	1s 	1s 

FIGURE 2.1: Electron configuration of carbon and its hybridizations.

Pure carbon occurs in several diverse forms (allotropes). Diamond is one of the carbon allotropes. Its atoms are arranged in a crystal structure shown in Figure 2.2 a) where each sp^3 hybridized carbon forms four equivalent σ bonds with neighboring atoms.

Crystal structure of graphene is formed by sp^2 hybridized carbon atoms arranged in hexagonal, honeycomb-like structure shown in Figure 2.2 b). The importance of this structure lies in the fact that other carbon sp^2 allotropes can be derived from it. Graphite is formed by graphene layers stacked on top of each other (Figure 2.2 e)). Its three-dimensional structure holds together due to weak van der Waals forces between individual layers. One dimensional carbon nanotubes can be seen as graphene rolled in one direction (Figure 2.2 d)). Fullerenes (zero-dimensional structures, Figure 2.2 c)) can be obtained from graphene by introducing pentagons into the spherically arranged graphene lattice [14].

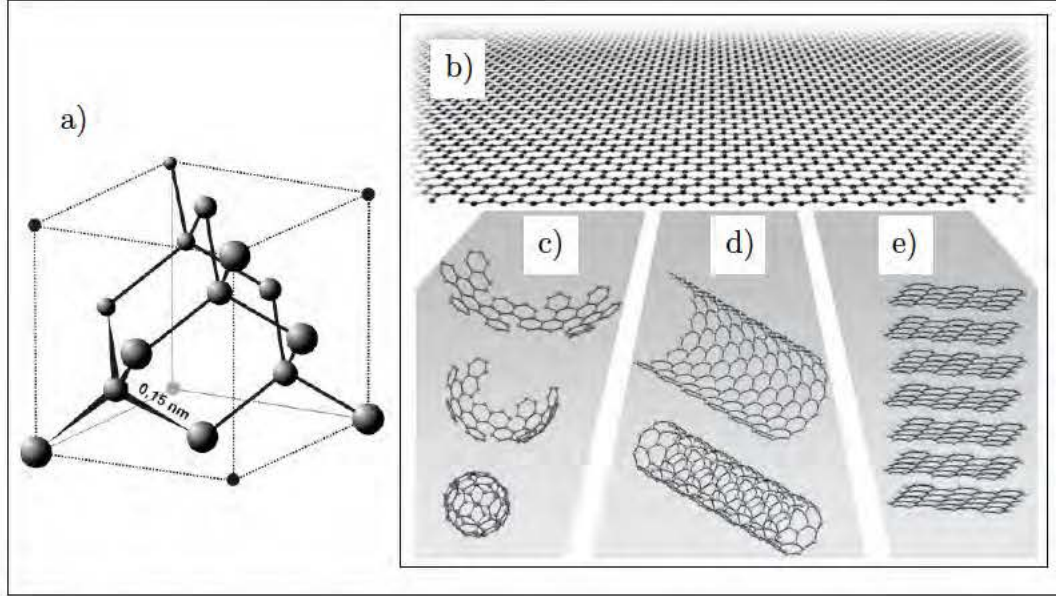


FIGURE 2.2: Structures of carbon allotropes. a) Diamond, b) graphene, c) fulleren, d) nanotube, e) graphite [15].

Although the two dimensional structure of graphene was theoretically described in 1946 [14], it only played the role of a theoretical concept for describing the other sp^2 allotropes. The individual graphene crystal was believed to be thermodynamically unstable because of thermal vibrations of carbon atoms which would lead to the breaking of carbon bonds. The existence of graphene layers is possible due to the warping of the graphene layer (Figure 2.4 a)) stabilizing the crystal lattice and allowing the existence of the single layer graphene at the room and higher temperatures.

2.1 Structure and electronic properties

The graphene crystal lattice is formed by two interleaving sublattices (A and B) forming the hexagonal, honeycomb-like structure (see Figure 2.3 a)). The vectors of the graphene unit cell are

$$\mathbf{a}_1 = \frac{a}{2} (3, \sqrt{3}), \quad (2.1)$$

$$\mathbf{a}_2 = \frac{a}{2} (3, -\sqrt{3}) \quad (2.2)$$

where $a \approx 1.42 \text{ \AA}$ is the distance of the nearest neighbors with lattice vectors

$$\delta_1 = \frac{a}{2} (1, \sqrt{3}), \quad (2.3)$$

$$\delta_2 = \frac{a}{2} (1, -\sqrt{3}), \quad (2.4)$$

$$\delta_3 = -a (-1, 0). \quad (2.5)$$

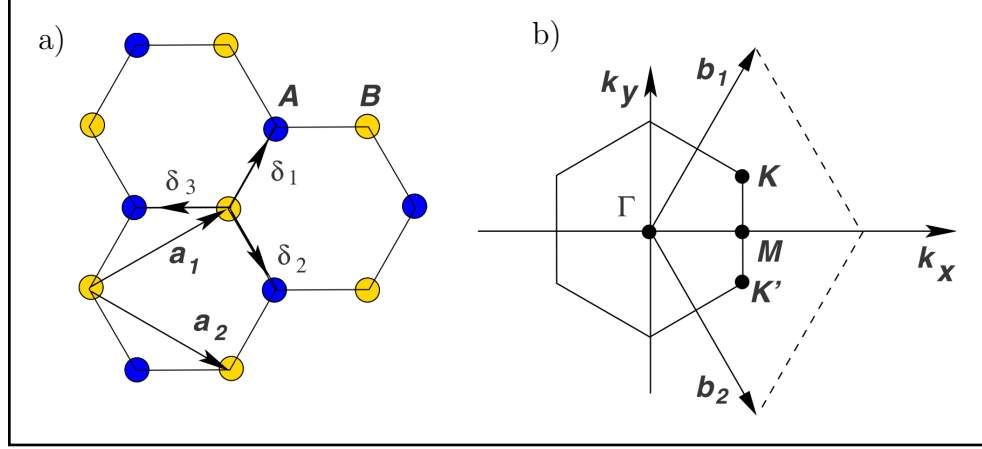


FIGURE 2.3: a) Graphene crystal lattice with the marked unit cell vectors and nearest-neighbor vectors, b) the first Brillouin zone and vectors of the reciprocal lattice [14].

The corresponding reciprocal lattice with vectors

$$\mathbf{b}_1 = \frac{2\pi}{3a} (1, \sqrt{3}), \quad (2.6)$$

$$\mathbf{b}_2 = \frac{2\pi}{3a} (1, -\sqrt{3}), \quad (2.7)$$

and the first Brillouin zone is shown in Figure 2.3 b).

The electrons from the hybridized sp^2 orbital of carbon atoms take part in the forming of strong σ -bonds with their three nearest neighbors. The p orbital with one remaining electron is oriented perpendicularly to the graphene planar structure and is unaffected by a σ -bonds forming. Delocalized electrons in the $2p_z$ orbitals lead to the formation of two π bands.

Mathematical description of the graphene band structure, which can be derived by the tight binding method, leads to the relation

$$E_{\pm}(\mathbf{k}) = \pm t \sqrt{3 + f(\mathbf{k})} - t' f(\mathbf{k}) \quad (2.8)$$

where

$$f(\mathbf{k}) = 2\cos(\sqrt{3}k_y a) + 4\cos\left(\frac{\sqrt{3}}{2}k_y a\right)\cos\left(\frac{\sqrt{3}}{2}k_x a\right), \quad (2.9)$$

t is the electron hopping energy to the nearest neighbor site (different sublattice), t' is a hopping energy to the second nearest neighbor (same sublattice) and $k_{x,y}$ represents corresponding components of the electron wave vector \mathbf{k} [14]. The plus sign refers to the conduction π^* band, minus sign to the valence π band.

The unique feature of the graphene can be seen from the graphical representation of its band structure shown in Figure 2.4 b): conduction and valence bands touch at Fermi level in points at the edge of the Brillouin zone, so called Dirac points. The position of these points in reciprocal space can be expressed by

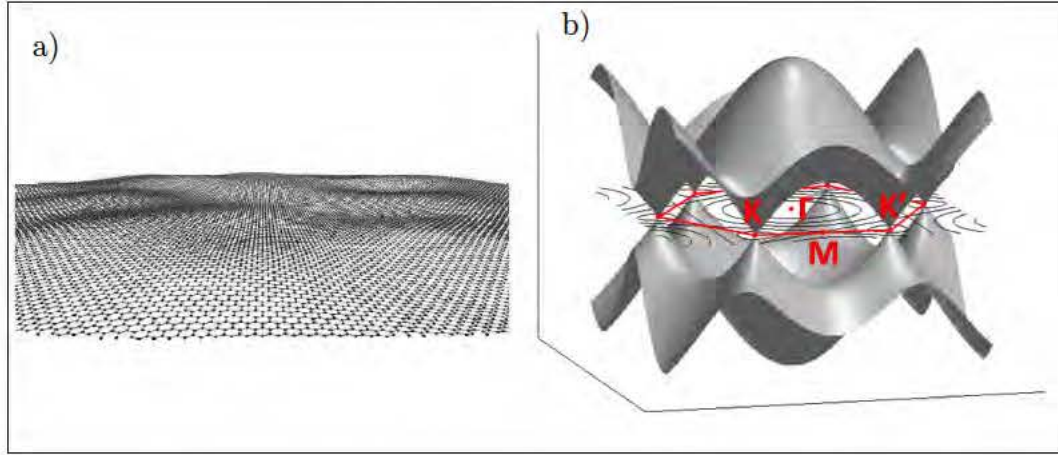


FIGURE 2.4: a) Intrinsic warping of the graphene crystal lattice [16], b) the band structure of graphene: valence π and conduction π^* bands touching at the Dirac points [17].

vectors

$$\mathbf{K} = \left(\frac{2\pi}{3a}, \frac{2\pi}{3\sqrt{3}a} \right), \quad (2.10)$$

$$\mathbf{K}' = \left(\frac{2\pi}{3a}, -\frac{2\pi}{3\sqrt{3}a} \right). \quad (2.11)$$

Due to its band structure, graphene can be formally classified either as a zero band gap semiconductor or a semimetal with a zero band overlap.

By expanding the equation 2.8 close to the Dirac point and assuming that $\mathbf{k} = \mathbf{K} + \mathbf{q}$ and $|\mathbf{q}| \ll |\mathbf{K}|$ we obtain a simplified relation

$$E_{\pm} = \pm \hbar v_F |\mathbf{q}| \quad (2.12)$$

where v_F is the Fermi velocity given by

$$v_F = \frac{3ta}{2\hbar} \cong 1 \cdot 10^6 \text{ m}\cdot\text{s}^{-1} \quad (2.13)$$

where t is the electron nearest neighbor hopping energy also found in (2.8) and a is the nearest neighbor distance. The linear dependence of energy on a wave vector in equation (2.12) differs from the quadratic dispersion typical for the electrons in solid state materials usually having form

$$E = \frac{|\mathbf{p}|^2}{2m^*} = \frac{(\hbar |\mathbf{k}|)^2}{2m^*} \quad (2.14)$$

where m^* is the effective mass of charge carriers and \mathbf{p} is the momentum vector. Another noticeable fact is that Fermi velocity in equation (2.12) does not depend on the mass of the electron which indicates that electrons in graphene act as relativistic massless particles called Dirac fermions. Behavior of these particles in graphene near the Dirac point reminds behavior of photons with dispersion

relation

$$E = \hbar\omega = \hbar c |\mathbf{k}| \quad (2.15)$$

where c is a velocity of light.

Instead of the Schrödinger equation used in standard materials for description of interaction of charge carriers with crystal periodic structure, a two-dimensional, relativistic Dirac equation is more convenient for the description of the behavior of charge carriers in graphene. The relativistic approach is applied even that the theoretical value of Fermi velocity in graphene is 300 times less than a speed of light and relativistic effects would not be normally taken into account.

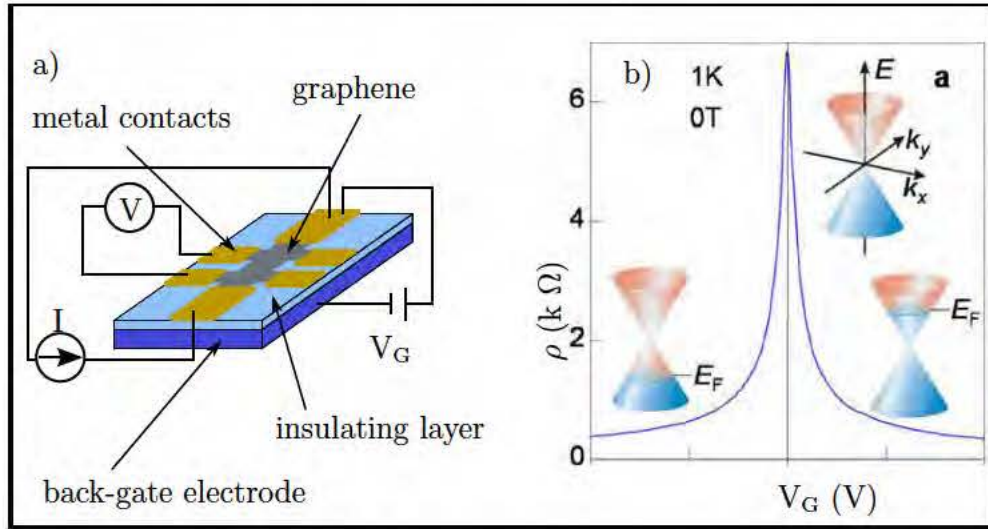


FIGURE 2.5: a) Schematic of the gate voltage measurement, b) dependence of graphene resistivity on the applied gate voltage. The Dirac point is located at $V_G = 0$ V. The insets show the position of the Fermi level [15].

Fundamental phenomenon of the electronic transport in graphene nanodevices is the ambipolar electric field effect of single layer graphene. This effect is observed when voltage is applied between the graphene layer and a gate electrode separated from graphene by an insulating layer (Figure 2.5). The Fermi level of pristine graphene lies at the crossing of valence and conductive bands (Dirac point) at zero gate voltage. When a positive gate voltage is applied, the conduction electrons concentration increases as a consequence of the Fermi level shift. This results in a decrease of the sample resistance. Similarly, negative gate voltage induces the Fermi level shift to lower energies and allows more hole states which also leads to the resistance decrease. In other words, graphene conductivity can be continuously switched between the hole type (p-type) and the electron type (n-type). Change of the position of the Dirac point and the consequent change type of conductivity at zero gate voltage can be also caused by graphene doping induced by, for example, the substrate [18], deposited material [19] or adsorbed impurities [20, 21].

2.2 Quantum Hall effect in graphene

When magnetic field is applied perpendicularly to the direction of a current flow in electric conductor, charge carriers are accumulated on one side of the conductor due to the magnetic part of the Lorentz force acting on them. Because of the charge accumulation, the potential difference across the conductor is induced causing electric force of the same magnitude as magnetic force acting on charge carriers in a direction opposite to magnetic force. The voltage generated across the sample is called Hall voltage and many practical sensing applications are based on its measurement.

By applying magnetic field perpendicularly to a two-dimensional electron gas (2DEG, electrons are confined in one direction) we can observe quantization of the Hall voltage. This phenomenon is referred to as the quantum Hall effect (QHE) and its discovery earned von Klitzing a Nobel prize in 1985 [22].

Electrons moving perpendicularly to the magnetic field \vec{B} are forced by the Lorentz force to move along circular trajectories called cyclotron orbits. In 2DEG systems, the values of energy associated with these orbits can take on only certain discrete values given by

$$E_N = \frac{\hbar e B}{m^*} \left(N + \frac{1}{2} \right) \quad (2.16)$$

where m^* stands for the effective mass of electrons, \hbar is the reduced Planck constant, e is the electron charge and N is an integer $N \geq 0$ [23]. These quantized levels are called Landau levels and their degeneracy is given by

$$\xi = 2 \frac{e B}{h} \quad (2.17)$$

where h is the Planck constant and number 2 occurs due to the spin degeneracy. It can be seen from equations (2.16) and (2.17) that with increasing magnetic field, the distance between Landau levels and their degeneracy increase and Landau levels are shifted relatively towards the Fermi energy. When Landau levels cross the Fermi level they get rid of electrons which drop to the lower Landau levels. These effects are observed as a discrete values of transverse resistance (quantum Hall effect, QHE) and by oscillations of longitudinal resistance (Shubnikov-de Haas oscillations, SdH) of the structure (see Figure 2.6).

Minima of longitudinal resistance correspond to the state where Fermi level lies between two Landau levels so the density of states at the Fermi level is minimal. When the highest Landau level gets near the Fermi level, states involved in charge carrier scattering occur. This leads to the increase of the longitudinal resistance and consequently to maxima in Figure 2.6 b). Discrete values of the transversal Hall resistance are

$$\rho_{xx} = \frac{h}{2ie^2} \quad (2.18)$$

where i is the filling factor expressing the number of completely filled Landau levels and the number 2 appears as a result of the spin degeneracy.

Although the electrons in graphene are also confined into two dimensions, the massless character of Dirac fermions causes that quantization of Landau levels

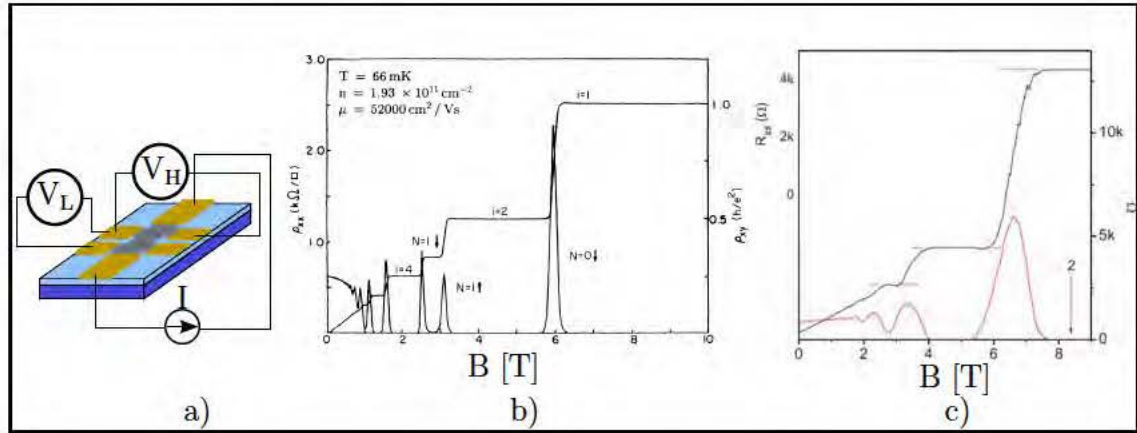


FIGURE 2.6: a) Schematics of the quantum Hall effect measurement, b) QHE and SdH oscillations in the 2DEG [24], c) QHE (black) and SdH oscillations (red) in graphene [25].

in magnetic field is somewhat different from the 2DEG case.

The energy of Landau levels in graphene are given by

$$E_N = \pm v_F \sqrt{2ehBN} \quad (2.19)$$

where $N \geq 0$ is an integer [26]. The plus sign in the equation 2.19 is valid for the electrons, the minus sign is valid for the holes. The Hall resistance ρ_{xx} in graphene takes on half integer values of quantum $h/4e^2$

$$\rho_{xx} = \frac{h}{4e^2(i+1)} \quad (2.20)$$

where i is an integer and the factor 4 appears due to the 4-fold degeneracy caused by spin degeneracy and double degeneracy caused by the existence of two graphene sublattices (graphene chirality).

In general, several conditions must be met in quantum Hall effect measurements. The magnetic field induced separation of Landau levels should be larger than Landau level broadening. This requires a presence of high magnetic fields and also high crystalline quality of the sample to attain minimal scattering rate of charge carriers. Moreover, low temperatures are usually needed to keep thermal energy much lower than Landau level separation. Despite the last mentioned fact, quantum Hall effect in graphene was observed during the room temperature measurement for high magnetic fields [27].

2.3 Raman spectra of graphene

Raman spectroscopy is a widely used analytical tool which provides information about rotational and vibrational spectra of studied systems. The basic physical principle of this technique is illustrated in Figure 2.7. Light of a specific wavelength impinges on the sample where it causes excitation of electrons from the ground state to the virtual energy level.

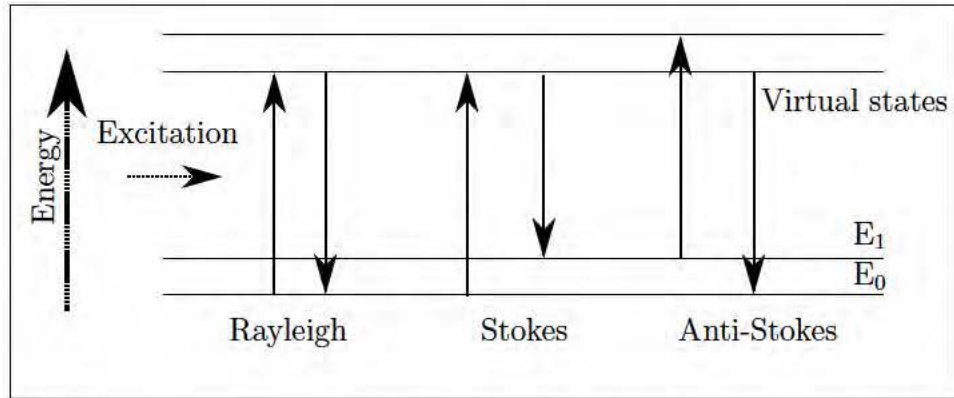


FIGURE 2.7: Schematic illustration of the Raman scattering process.

When the excited electron returns back to the ground state, photon emitted during this process has the same wavelength as the incident light. This process is called Rayleigh scattering. The process where initial and final state of the electrons are different is called Raman scattering. When the electron returns from excited to higher (vibrational) energy level, wavelength of the emitted photon is shifted to higher value (i.e. lower energy) with respect to the incident light (Stokes shift). In analogy, when the final (vibrational) level is lower than the initial state of electron, wavelength of emitted photon is shifted to higher energies (anti-Stokes shift).

Typical spectrum of graphene with its characteristic features is shown in Figure 2.8. The peak located at $\sim 1580 \text{ cm}^{-1}$ is called G peak and it is common sign of carbon sp^2 materials. The so called 2D peak is located at $\sim 2700 \text{ cm}^{-1}$ and for single layer graphene is typical its narrow shape and high intensity. The D peak which could be found at $\sim 1350 \text{ cm}^{-1}$ (Figure 2.9) arises from defects and disorder in crystal lattice of graphene and it is not observed in a Raman spectrum of high quality graphene.

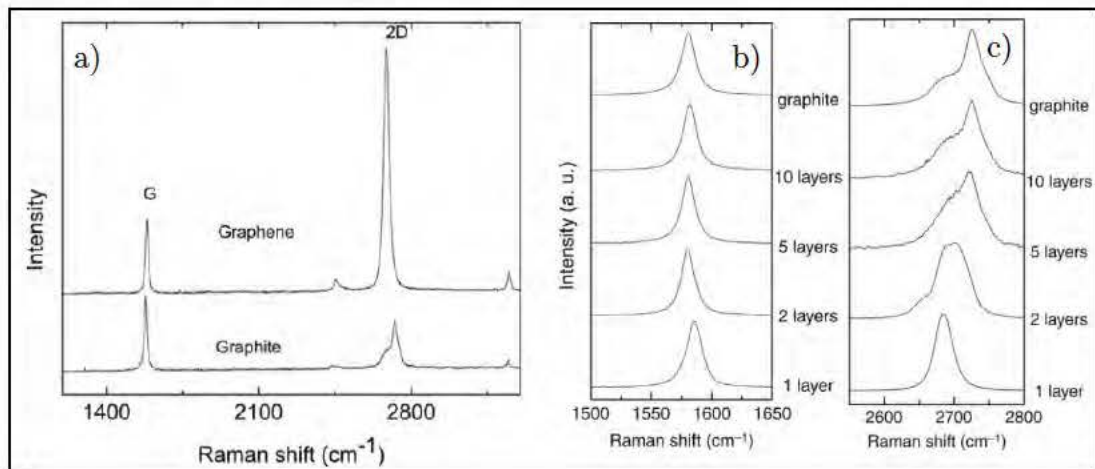


FIGURE 2.8: a) Typical Raman spectrum of graphene, b) G and c) 2D peaks for different numbers of graphene layers. [28].

Raman spectroscopy is frequently used to examine the quality of graphene layers by determining the intensity of the D peak. Moreover, Raman spectroscopy

is capable of distinguishing between the number of graphene layers on the sample. The shape of the 2D peak changes from narrow and symmetric for single layer to broad asymmetric peak of lower intensity for graphite. Also the position of the G peak is slightly shifted (see Figure 2.8 b), c)). In addition, the ratio of intensities G/2D for single layer graphene increases with the number of stacked graphene layers (see Figure 2.9 b)). Nevertheless, the Raman spectra of graphene depend on many factors and direct comparison is relevant only for spectra taken with the same instrument setup, type of the substrate, excitation laser wavelength etc.

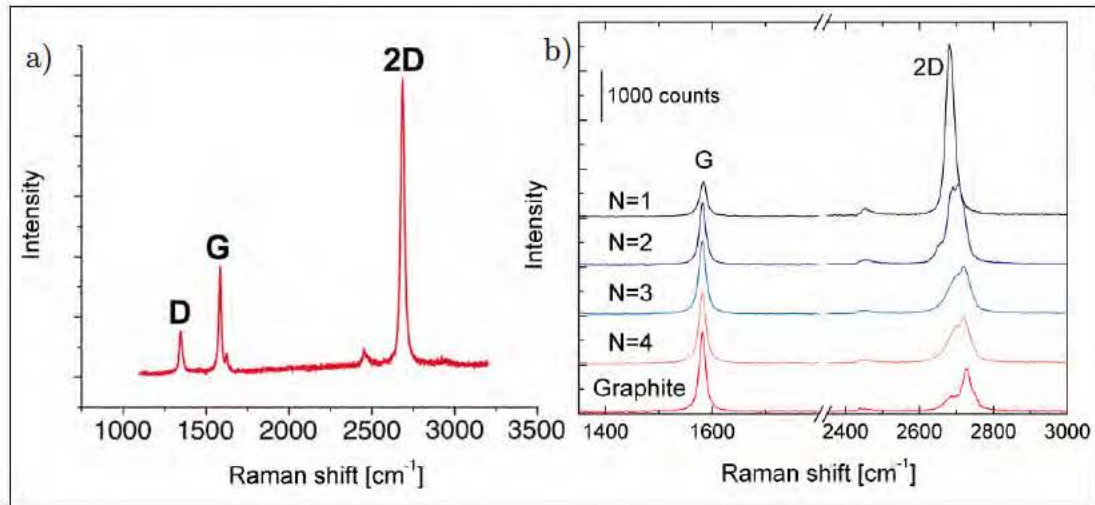


FIGURE 2.9: a) Raman spectrum of graphene containing defects [29], b) the Raman spectra for different number of graphene layers [17].

Chapter 3

Graphene Preparation Methods

There are several ways to produce graphene. The first method used for the preparation of graphene samples was the mechanical exfoliation (also known as *Scotch tape* method)[1]. This method is based on a mechanical cleaving of graphene flakes from highly oriented pyrolytic graphite by adhesive tape and consequent transfer of these flakes from the tape to the target substrate.

Although high quality flakes of a single-layer graphene are produced this way, mechanical exfoliation is not suitable for large scale production of graphene layers due to its very low reproducibility. Nevertheless, the scotch tape method remains commonly used technique for prototyping of graphene nanodevices in basic research [30] since the exfoliated graphene flakes have excellent electronic properties.

During liquid-phase exfoliation, cleaving of graphite into graphene flakes is induced by sonication. That results into a suspension of submicrometer sized graphene flakes. Obtained graphene suspension can be used to deposit polycrystalline graphene layers. The efficiency of the ultrasonic cleavage can be enhanced by chemical intercalation. An alternative approach starts with oxidized graphite which is cleaved into the graphene oxide (GO). Deposited graphene oxide layers can be partially reduced back into the graphene state (reduced graphene oxide - rGO) by, for example, chemical treatment or direct heating [31]. Typical applications considered for GO and rGO layer are related with functional coatings, composite materials or biological applications [10, 11].

Epitaxial graphene layer can be grown on the silicon carbide (SiC) surface. Heating of the SiC crystals at high temperature (1500 °C– 2000 °C) in an argon atmosphere or in ultra high vacuum leads to sublimation of silicon atoms and subsequent formation of graphene layer on the surface. This method produces high quality graphene layers suitable for fabrication of high-frequency transistors [4].

Another method for graphene deposition is called Chemical Vapor Deposition (CVD). This method is the main subject of this thesis and it will be discussed in more details in the following section.

Unzipping of carbon nanotubes, molecular beam epitaxy and laser ablation deposition belong to the less frequently used approaches for the graphene preparation. Nevertheless, these methods have been shown as interesting alternatives to the more standard techniques [2].

3.1 Chemical vapor deposition

CVD employs hydrocarbon gas as a source of carbon atoms for the graphene synthesis. Methane is the most widely used feedstock gas (also used in this work) but other ones like acetylene [32], ethylene [33] or toluene [34] are also studied. The scheme of the typical graphene CVD furnace is shown in Figure 3.1. The main part of the deposition system consists of the quartz tube with the heating stage. The tube is connected to the pumping system on one side and to the gas supply on the other. The quartz tube with the substrate inside is pumped, heated to high temperatures ($700^{\circ}\text{C} - 1100^{\circ}\text{C}$) and filled with reaction gases (CH_4 , H_2).

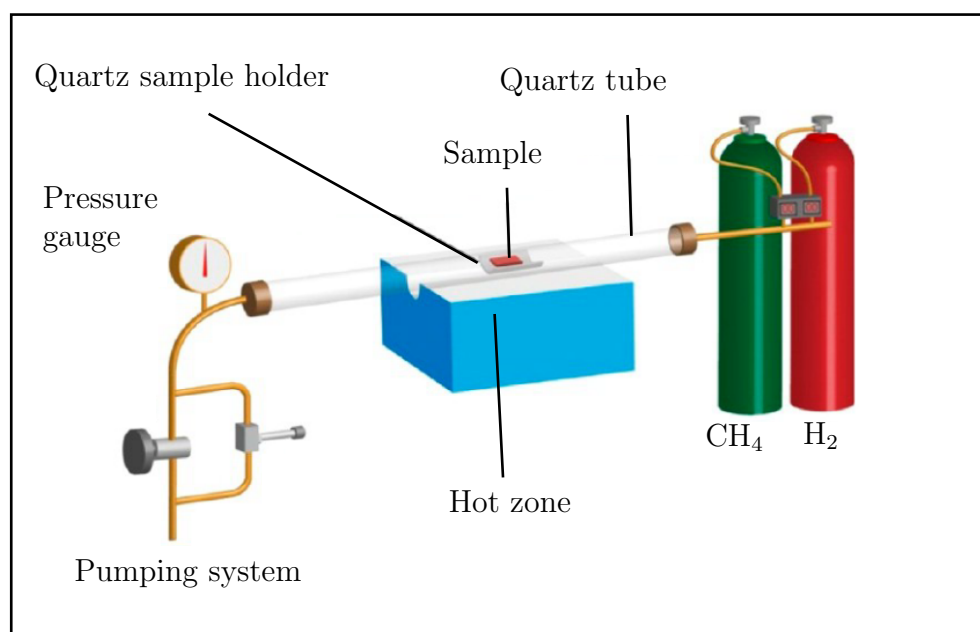


FIGURE 3.1: Schematic of the chemical vapor deposition system, adapted from [35].

In the first step of graphene CVD, the hydrocarbon gas (in this case methane) is decomposed to carbon and hydrogen molecules. Due to strong C-H bonds in methane, direct thermal decomposition occurs at temperatures in excess of 1000°C [36] and can be run efficiently at $1500^{\circ}\text{C} - 2000^{\circ}\text{C}$ [37]. The result of this reaction is carbon black, which is, in fact, chaotically connected carbon flakes. At the temperatures above 3000°C , bulk graphite growth can be performed [38]. Lower activation energy of methane decomposition can be achieved by using a transition metal serving as a catalyst. This allows the reaction to run efficiently at lower temperatures. In CVD of graphene, transition metal catalyst serves also as a substrate for graphene.

The graphene growth mechanism is strongly influenced by the type of the used substrate. CVD of graphene has been demonstrated on various transition metals like Ru, Ir, Co, Re, Pt, Pd, Fe, Au, Ni, Cu and Cu-Ni, Au-Ni or stainless steel alloys [39, 40]. The catalytic abilities of transition metals and some of their alloys, which comes from their partially filled electron d-orbitals, provide low energy paths to the reaction process [39]. One of the important properties of the

substrate/catalyst is its affinity to carbon, which defines the ability of material to form carbides and its carbon solubility. These factors, together with growth conditions, determine the graphene growth mechanism.

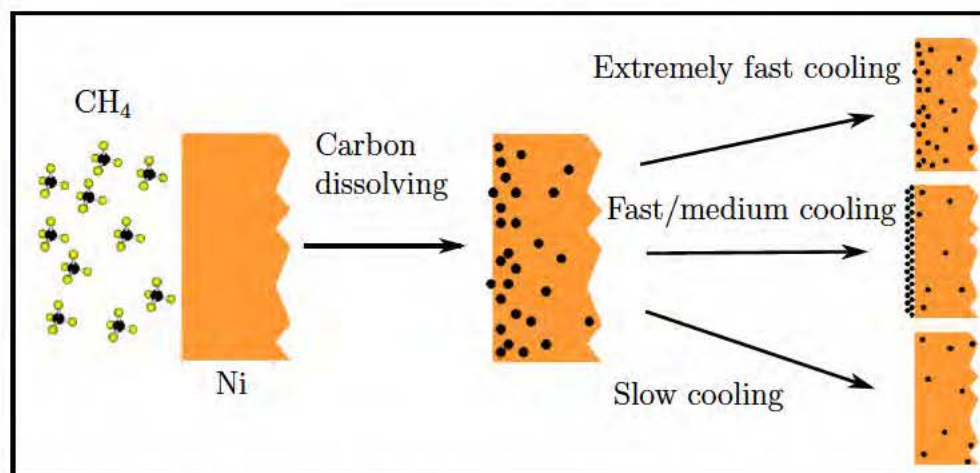


FIGURE 3.2: CVD process of graphene synthesis on a nickel substrate, adapted from [41].

There are two basic mechanisms of the graphene CVD growth: graphene forming from carbon precipitated from the substrate and graphene forming from adsorbed carbon species on the surface. The first mechanism is typical for the nickel which has relatively high carbon solubility at elevated temperatures [42]. During the deposition, carbon atoms coming from the methane decomposition diffuse into the nickel substrate. When the nickel is cooled down, carbon solubility of nickel decreases and carbon precipitates to the surface. Setting the optimal cooling rate leads to the graphene formation (monolayer or multilayer) on the surface of the nickel substrate. Basic scheme of graphene forming on nickel substrate is shown in Figure 3.2.

The second type of the graphene growth is usually observed on the copper substrate. Copper is characteristic by a very low carbon solubility even at high temperatures. Therefore, carbon species produced by the catalytic decomposition do not diffuse to the bulk and stay on the surface where they can nucleate and form graphene layers. The scheme of processes taking place on copper during graphene deposition is shown in Figure 3.3. The process marked as (1) illustrates the methane catalytic decomposition which provides carbon atoms for graphene formation. This process is accompanied by the adsorption and desorption of CH₄ molecules. Hydrogen assisted dehydrogenation of CH₄ occurs at a presence of H₂ and also supplies carbon species to the process. This mechanism becomes dominant when the Cu surface is mostly covered by graphene and it is not accessible for CH₄ molecules.

Process (2) represents the temperature activated surface diffusion of carbon species (monomers or clusters) which do not desorb and stay on the Cu substrate.

Nucleation of graphene domains is illustrated in Figure 3.3 as (3). Nucleation centers of graphene domains can be formed on Cu grain boundaries, surface roughness features, crystalline local defects or surface impurities. After the CH₄ exposure, the carbon species concentration on the Cu surface is increasing. When

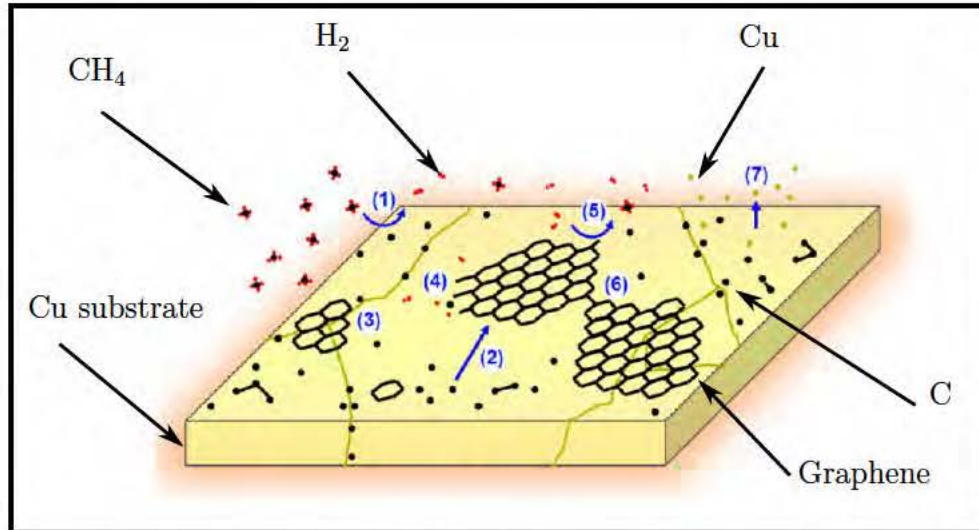


FIGURE 3.3: Schematic of the surface processes during the graphene growth on a copper substrate. 1) Catalytic decomposition of CH_4 , 2) surface diffusion of C atoms, 3) graphene nucleation, 4) growth of graphene domains, 5) graphene etching by H_2 , 6) coalescence of graphene domains, 7) Cu sublimation. Adapted from [43].

it reaches certain value (supersaturation level), formation of stable nucleus takes place. The concentration of carbon species is decreased under the critical value and nucleation rate is negligible during the rest of the deposition [44].

During the deposition, graphene single-crystalline domains around nucleation centers get larger ((4) in Figure 3.3) and they eventually stitch together (see Figure 3.6 b) to form continuous polycrystalline layer by coalescence of neighboring domains (process (6)). As a result of this process, graphene domain boundaries are formed on the borders of merging single domains. Graphene domains can be found in variety of shapes which are dependent on several parameters (see Figure 3.4).

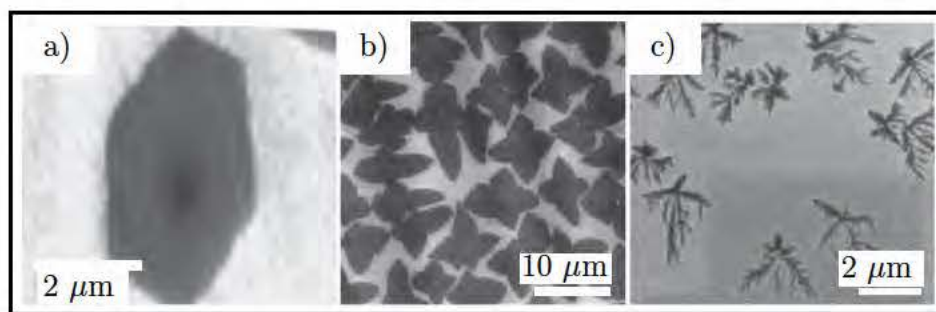


FIGURE 3.4: Examples of graphene domain shapes: a) hexagonal, b) four lobed, c) dendritic shape. Adapted from [45].

Process (5) shown in Figure 3.3 represents hydrogen etching of graphene as a reverse reaction to carbon decomposition. Etching occurs predominantly on the edges of graphene domains where the C-C bonds are weaker.

Another process occurring during the deposition is a sublimation of Cu atoms (Figure 3.3). This is caused by high deposition temperatures which are close to

the copper melting temperature (1084 °C). Cu sublimation is more significant at low deposition pressures ($< 10^2$ Pa) and can increase surface roughness of the substrate [46].

Graphene grown on copper typically contain defects as cracks, wrinkles, bi-layer areas and uncovered Cu areas. The origin of wrinkles comes from different thermal expansion of Cu (positive) and graphene (negative). Mechanical stress induced during cooling of the Cu is released via formation of wrinkles [39]. Examples of defects of graphene grown on a polycrystalline Cu foil are shown in Figure 3.5

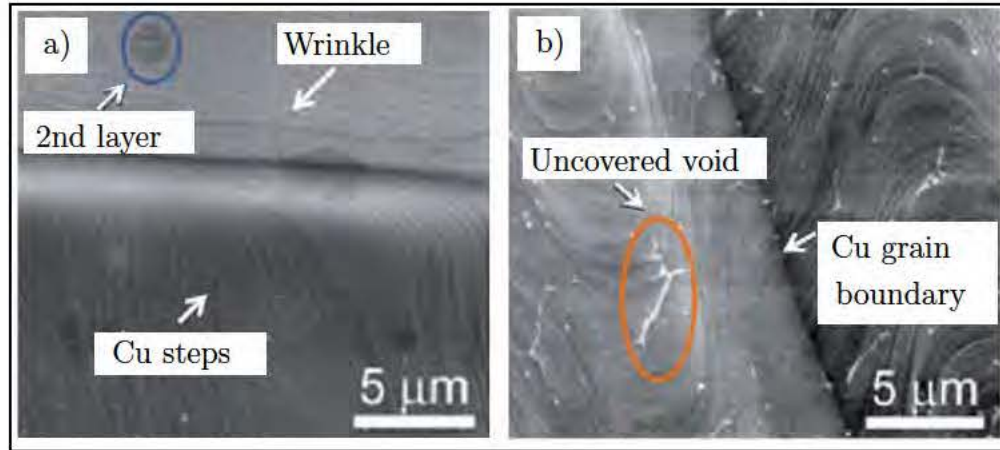


FIGURE 3.5: Examples of graphene defects on the Cu foil, a) wrinkle, graphene second layer, b) a void caused by not connected graphene domains, Cu grain boundary, adapted from [39].

3.1.1 Types of Cu substrates

As it was mentioned above, graphene layers produced by CVD contain domain boundaries. These defects negatively effect electrical transport properties of graphene because they act as scattering centers for charge carriers [47]. Therefore, to obtain high quality graphene layers, it is crucial to grow graphene with minimum of grain boundaries. This can be achieved by minimizing the number of graphene nucleation centers which leads to the graphene layer consisting of a small number of large graphene domains merged together. In the ideal case, the resulting layer would consist of just one graphene single-crystal grown from one nucleation center. Reduction of the grain boundaries can lead to CVD graphene with electronic transport properties comparable to exfoliated graphene [48].

The nucleation density of graphene strongly depends on the type and condition of a substrate. The substrate with minimum nucleation probability should contain minimum surface impurities, grain boundaries, crystalline defects and has very low surface roughness. According to this, the most convenient substrate to achieve large graphene single domains would be a high quality Cu single crystal. On the other hand, relatively complicated manufacture and high cost of Cu single

crystals do not make them acceptable choice for a graphene mass production. Nevertheless, they are useful for experiments investigating basic principles of graphene growth and influence of crystalline orientation of a substrate [49–51].

An alternative to the single crystal substrates are thin copper films deposited on insulating substrates [52–54]. Even that sputtered or evaporated Cu films on sapphire, magnesium oxide or quartz crystal are of a lower crystalline quality than Cu single crystals, they have been shown as convenient substrates for graphene CVD and they have advantage in lower cost.

Although cold-rolled thin copper foils does not seem as an ideal candidate for a substrate due to their polycrystalline nature and high surface roughness, they have been widely used mainly because of their high availability and low cost compared to other alternatives.

3.1.2 Role of the crystallographic orientation of the substrate

It has been shown that properties of graphene domains can be influenced by a crystallographic orientation of the underlying substrate. Different characters of the graphene growth for different concentration arise from different nucleation sites, adsorption, and diffusion energies for different orientations of Cu grains [45]. For graphene growth on copper, there are two significant crystallographic orientations of Cu grains with respect to the surface: Cu(111) and Cu(100). It has been observed that Cu(111) promotes uniform growth of predominantly monolayer graphene in contrast to Cu(100) which shows slower graphene growth of more defective and multilayer graphene [49, 55]. Crystalline orientation of Cu grains can also influence the alignment [56] and the shape [57] of graphene single domains. Graphene domains with four-folded symmetry shapes were found on the Cu grains with four fold symmetry (e.g. Cu(100)) and graphene domains with six-folded symmetry were found on the Cu grains with six-folded symmetry (e.g. Cu(111)) (see Figure 3.7). Relatively weak interaction between graphene and Cu substrate allows graphene domains to grow over Cu grain boundaries with minimal structural defects [39, 58] (Figure 3.6 a)). The shape of graphene domains is also determined by other parameters. At certain conditions (usually high deposition pressure), shapes of graphene domains do not seem to be affected by the symmetry of the substrate [58, 59]. The influence of different crystallographic orientations on graphene growth is also less significant at temperatures above 1000 °C [46].

3.1.3 Role of substrate roughness and surface impurities

Roughness of the substrate is one of the key factors affecting graphene nucleation. High surface roughness is connected with high nucleation density and, in a consequence, smaller graphene domains. The surface roughness of widely used copper foils is caused by cold rolling manufacturing process. To lower the level of roughness, predeposition treatment like electropolishing could be employed [44].

Dhingara et al. presented interesting approach to reach a smooth surface of a Cu substrate [60]. Instead of thin copper foils, they used thick copper disk with a surface polished by precise diamond machining. The roughness of these

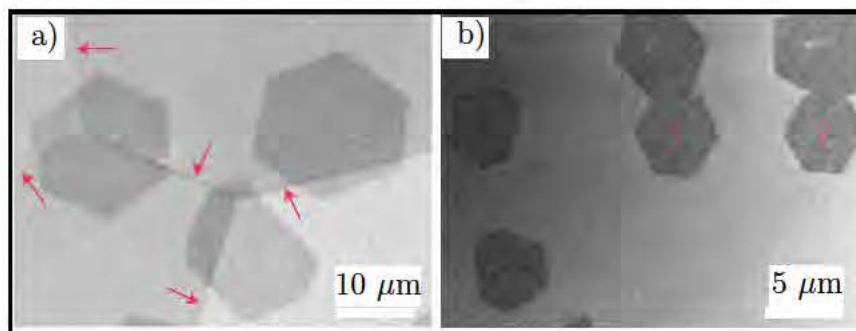


FIGURE 3.6: a) Graphene domains overgrowing a Cu grain boundary marked by the red arrows, b) connecting of individual graphene domains and formation of domain boundary (numbers 1 and 2), adapted from [58].

substrates was estimated 50 times lower than of thin electropolished Cu foils and resulted in graphene domains of sizes approaching $70\text{ }\mu\text{m}$.

Another method was developed within the Institute of Physical Engineering by Procházka et al. [61]. Their substrate consists of the thin copper film sputtered on 280 nm SiO_2 on Si substrate. Afterwards, the supporting copper layer was electrochemically deposited on the top of the sputtered film. The copper was then stripped from the SiO_2 template. The topography of this Cu foil from the side peeled off from the template copies the topography of the flat SiO_2 . The roughness of such substrate is much lower than the roughness of the commercial copper foils even after high temperature annealing. These smooth foils exhibited low graphene nucleation density and graphene layers possessed higher electron mobilities compared to graphene grown on standard commercial foils.

Surface impurities can increase catalytic activity happening on the Cu surface and they can increase nucleation density of graphene. Liu et al. observed forming of second layer graphene regions on low purity copper foils (99.8 %) in contrast with predominantly monolayer graphene on high purity Cu foils (99.999 %) [62].

Before the deposition, native oxide covering the Cu foil is removed by annealing at high temperature in the presence of hydrogen serving as a reducing agent. This process also leads to an enlargement of the Cu grains, although, according to several reports, the size of the Cu grains does not influence the size of the grown graphene domains [45].

Oxygen is a special case between the surface impurities on copper. Gan et al. published the deposition of large graphene domains forming on the Cu foil after annealing without hydrogen [59]. After the annealing, they observed presence of nanoparticles serving as the graphene nucleation seeds. Origin of these nanoparticles was assigned to the trace amount of oxygen in the argon gas. Hao et al. reported a synthesis of the graphene single domains of the size in the orders of millimeters by annealing the Cu foil in the low partial pressure of oxygen before the deposition. Oxygen atoms adsorbed on the Cu surface during the annealing can passivate available nucleation sites and thus dramatically reduce the graphene nucleation density [63].

3.1.4 Role of the deposition temperature

Temperature is an important factor affecting the catalytic decomposition, adsorption and desorption of the molecules on the Cu substrate, surface diffusion of carbon species and Cu sublimation (at low pressures). Higher deposition temperatures (~ 1000 °C) lead to lower nucleation density and larger graphene domains compared to lower temperatures (< 900 °C) [44, 62]. At low temperatures, lower efficiency of CH_4 decomposition causes that the carbon supply to graphene domains is not sufficient to allow merging of the graphene domains and formation of continuous graphene layer [44].

3.1.5 Role of the deposition pressure and reaction gases partial pressures

CVD of graphene can be divided into two groups according to the deposition pressure: Low Pressure CVD (LPCVD) and Atmospheric Pressure CVD (APCVD). LPCVD is usually characterized by using deposition pressures below 100 Pa. Low pressure in combination with high deposition temperature allow Cu sublimation to occur. As a result, the roughness of the substrate is increased, which could affect uniformity of graphene layer. On the other hand Cu evaporation could also promote desorption of carbon species from the Cu surface, lower their surface concentration and thus reduce graphene nucleation density [46]. According to suggested mechanisms and experimental observation, LPCVD graphene growth is predominantly surface activated and thus self limiting [32]. This means that when the Cu substrate is completely covered, growth does not continue and grown graphene is highly uniform and mostly monolayer [64].

APCVD employs, apart from CH_4 and H_2 , inert buffer gas (typically argon) for a better pressure control. Copper sublimation is dramatically reduced during APCVD which leaves the substrate smoother than in LPCVD case. In addition, desorption of carbon species is partially suppressed and has different activation energy due to the absence of Cu sublimation [46]. Compared to LPCVD, APCVD graphene growth on copper has not been found self-limiting and produced layers can be nonuniform and contain multilayer regions [45]. It has been reported, that graphene growth mechanism during APCVD can be described, despite low carbon solubility in Cu, as a diffusion and precipitation driven contrary to the surface activated growth during LPCVD [32]. Nevertheless, uniform monolayer graphene can be deposited at the atmospheric pressure by adjusting other deposition parameters [64]. The advantage of APCVD is that it does not require complicated vacuum system as LPCVD and it is thus more favorable for an industrial usage.

The ratio of CH_4 and H_2 in reaction chamber has significant influence on graphene growth. With increasing CH_4/H_2 ratio (increasing partial pressure of CH_4), the shape of graphene domains change from compact to more fractal-like patterns [57] (see Figure 3.7). The shape of the domains is influenced by the relation between domain edge attachment and diffusive mass transport of carbon species around the edges of the domain. When the CH_4 partial pressure is low, the concentration of available carbon species is low and the rate limiting factor of graphene growth is the edge attachment rate. Under these conditions, graphene

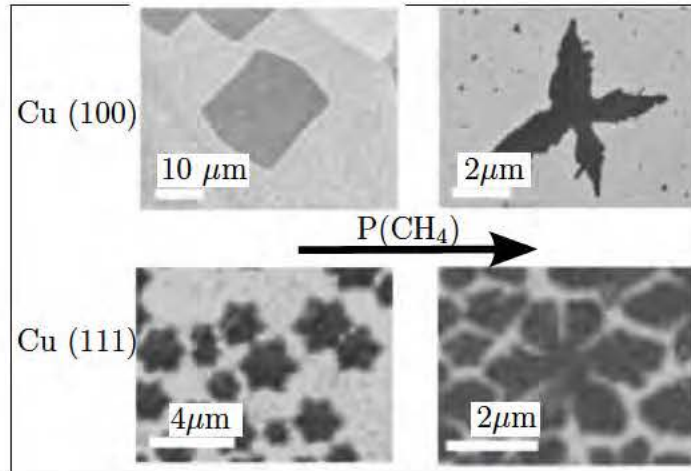


FIGURE 3.7: Examples of graphene domain shapes on different crystallographic orientation of the Cu substrate and the influence of CH_4 partial pressure. With the increasing partial pressure of methane the graphene domains change their shape from compact to dendritic. Adapted from [57].

domains have compact shape. When the CH_4 concentration is increased, the edge attachment rate is increased and the diffusive mass transport of carbon species becomes the limiting factor of the graphene growth. As a consequence, the shape of graphene domains becomes dendritic with fractal-like edges [63].

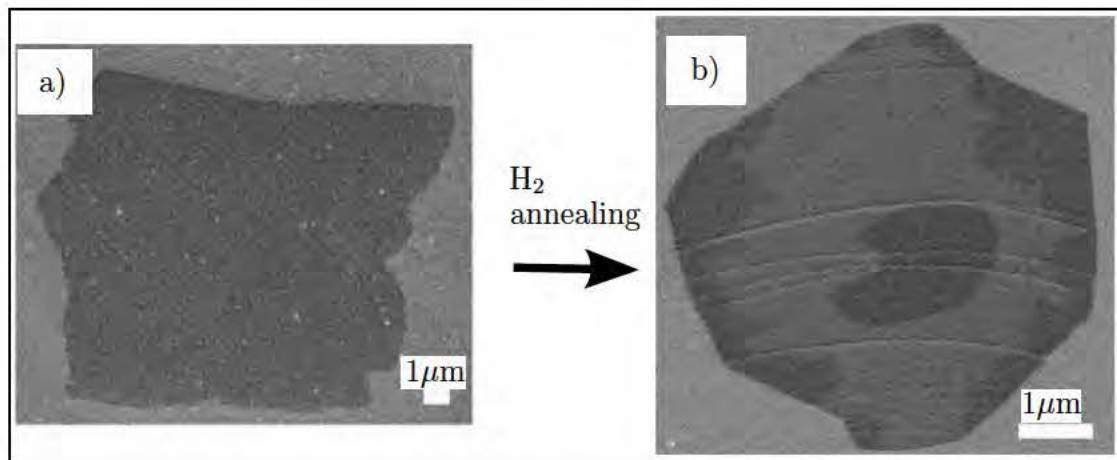


FIGURE 3.8: Demonstration of hydrogen etching of a graphene domain. Adapted from [65].

It was also reported that lower partial pressures of methane leads to lower nucleation density and larger graphene domains [35]. These observations can be interpreted taking into account the roles of CH_4 and H_2 during the deposition. When CH_4 supply is reduced, the probability of methane adsorption and decomposition decreases. As a consequence, the concentration of carbon species on the surface gets lower and nucleation density is reduced because graphene nucleation occurs more likely at higher carbon concentrations [43, 62]. Higher concentration of carbon species also promotes faster growth rate of graphene.

Apart from the role of hydrogen during substrate predeposition annealing, there are some other functions assigned to hydrogen during graphene growth. As mentioned earlier, one of them is co-catalyst effect on decomposition of hydrocarbon gas by means of H_2 assisted dehydrogenation. Hydrogen has also the ability to remove active carbon species from the surface and to etch weak C-C bonds located at the edges of graphene domains and thus to reduce their growth ability and change their shape [43] (Figure 3.8). On the other hand, in the work published by Choubak et al., no hydrogen etching of graphene was observed in the purified hydrogen which led them to conclude that oxidizing impurities in hydrogen are responsible for graphene etching rather than hydrogen itself [66]. Vlassiounk et al. has reported, that graphene growth rate has a maximum for partial pressure of hydrogen about 200 – 400 times higher than methane partial pressure [65]. Liu et al. have shown, that minimal partial pressure of CH_4 is necessary to achieve full graphene coverage [62]. In some cases, the presence of hydrogen during the growth can induce point defects to graphene and high partial pressures of hydrogen can destroy self-limiting nature of graphene and leads to formation of multilayers [45].

Despite of great number of scientific studies focused on the CVD growth of graphene on copper, the precise mechanism of graphene growth has not been fully elucidated yet. As it was described above, this process is influenced by many different factors which determine the properties of the graphene layer. Variety of diverse results coming from different scientific groups imply that there is no generally applicable receipt for deposition of high quality graphene layers. On the other hand, the technique for growing large scale, high quality graphene layers is highly desirable and the progress achieved in graphene CVD in the last years makes this method very promising for the future.

3.1.6 CVD Modifications

Several modifications of the standard graphene CVD are known. Tao et al. developed a method resulting in high electron mobility in graphene where the Cu substrate is heated by electromagnetic induction [67]. A change in behavior of the graphene growth was observed in experiments where Cu substrate was placed into additional quartz tube with one closed end inside the deposition system, which changed the gas flow path and composition near the substrate [68, 69].

Improvement of graphene quality was also achieved in setups using encapsulation and covering of the Cu foil during LPCVD which lead to the redeposition of evaporated copper [70, 71]. Cu vapors also play a role in the study [72], when graphene was deposited directly on the SiO_2 substrate and the CH_4 catalytic decomposition was carried out mainly by the Cu vapors. Other method is based on noncatalytic decomposition of CH_4 . The graphene is deposited directly onto an SiO_2/Si substrate without using any catalyst but achieved quality is not competitive with the standard CVD [38].

3.1.7 Graphene Transfer

After the CVD deposition, graphene is located on the surface of the used transition metal catalyst. Therefore, transfer of these layers onto an insulating

substrate is necessary for further utilizing of graphene layers for any application. Graphene transfer is, with the deposition, the factor determining the quality and performance of graphene devices. Hence, the optimal handling of the transfer procedure to achieve low transport caused degradation of graphene is an current topic in graphene CVD research.

In the typical CVD graphene transfer, a polymer layer (e.g. Poly(methyl methacrylate) - PMMA) is deposited on the one side of the copper foil. Function of this layer is to support and protect the graphene layer during the transfer process. The transfer procedure can be also performed without the supporting layer but it requires more delicate and careful handling and tearing of graphene layer is very likely to occur during the process. Cu foil is then etched away by copper etching solution (FeNO_3 , FeC_3 , HNO_3 ,...) and PMMA/graphene structure is placed on the insulating substrate (e.g SiO_2/Si).

Polymer residues remaining on graphene after supporting layer removal cleaning are the big drawback of the described transfer method. The presence of the residues can cause unintentional doping of the graphene and degrade its electronic transport properties [73]. PMMA can be partially removed by annealing in vacuum. However, certain amount of PMMA residues were found on graphene even after the annealing process [74]. Vacuum annealing of graphene at temperatures close to 400 °C can also significantly damage graphene layers [75] and so lower annealing temperatures must be employed.

Contacts for graphene devices are manufactured by electron beam lithography and metal sputtering. The standard wet transfer process and contact manufacturing were employed in the frame of this thesis and they are described in more details in section 4.1.2.

Chapter 4

Experimental setup and methods description

This chapter briefly describes methods and instruments used in the experimental work presented in chapter 5. All experiments were, with two exception, conducted in clean room laboratory of IPE FME BUT.

4.1 Chemical Vapor Deposition system and transfer technology

Chemical Vapor Deposition of graphene was carried out in home-build deposition system shown in Figure 4.1. The system and the deposition technology were developed as a part of master thesis of Pavel Procházka [76].

4.1.1 Deposition system

The main part of the system consists of a quartz tube with a resistive heating wire (FeCrAl alloy) wound around. Both parts of the quartz tube are sealed by Viton ring pressed between the outer surface of the tube and sealing flanges. One side of the tube is connected to the pumping system consisting of a turbomolecular pump and a scroll pump serving as a backing pump. The other side of the tube is connected to reaction gas supply system with H_2 and CH_4 gas cylinders at the end. Flows of the gases incoming to the reaction chamber are controlled by Mass Flow Controllers (MFCs) placed on each gas line. The pressure inside the chamber is controlled by adjusting the pumping speed via control valve connected to the inlet of the turbomolecular pump. For measuring the pressure, both Pirani gauge and Baratron gauge are employed to cover broad pressure range.

Two types of the system described above were employed for the deposition. The first system was made from the 10 cm diameter quartz tube. Due to the cracking of the tube during the maintenance the system was exchanged for a smaller system with 5 cm diameter quartz tube.

Part of the deposition system is the sample holder shown in Figure 4.2. Cu foil is attached to the sample stage of the holder and it is supported by molybdenum metal sheet. R-type thermocouple is placed on the bottom side of the

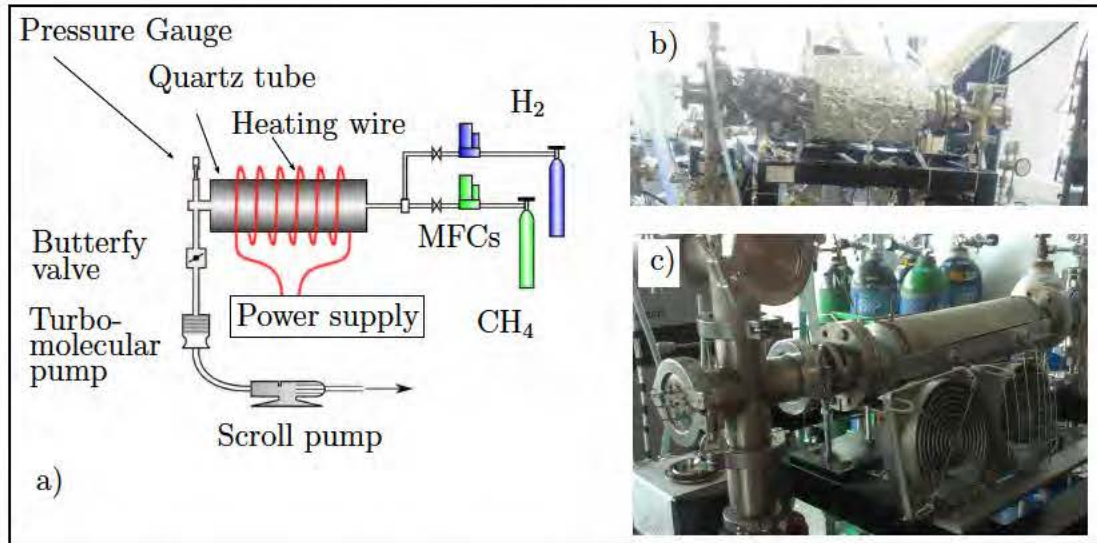


FIGURE 4.1: a) Schematic of the home-built CVD system and b) picture of the 9.5 cm inner diameter furnace (adapted from [76]) which was later exchanged for c) the 4.5 cm inner diameter furnace.

construction. This sample holder was used only in the beginning of the deposition series and it was removed from reasons described in section 5.2.

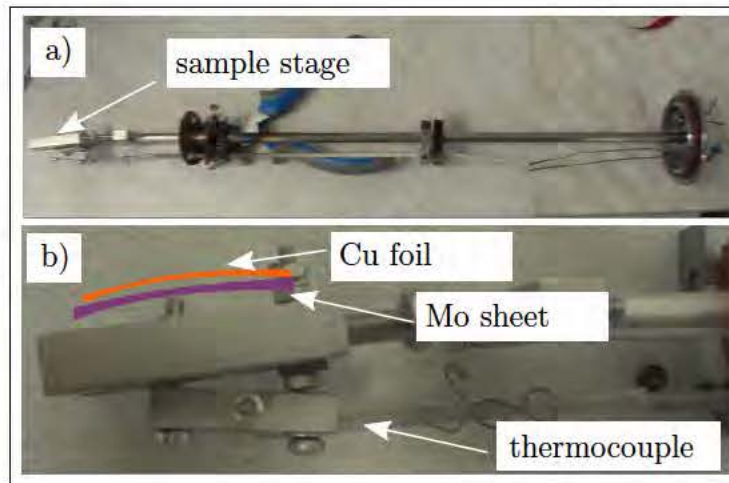


FIGURE 4.2: a) CVD system sample holder, b) a detail of the sample stage, the Cu foil is supported by molybdenum metal sheet.

4.1.2 Graphene Transfer and Contacting

The scheme of the transfer process is shown in Figure 4.3. in the first step, thin layer of PMMA (~ 300 nm) is spincoated on one side on the Cu foil to support the graphene layer during the transfer procedure.

In the second step, graphene grown on the bottom side of the Cu foil (side not covered by supporting layer) is removed by etching in oxygen plasma etching (2 minutes, 80 % Ar, 20 % O₂). This task was performed by the instrument Diener Nano Plasma stripper.

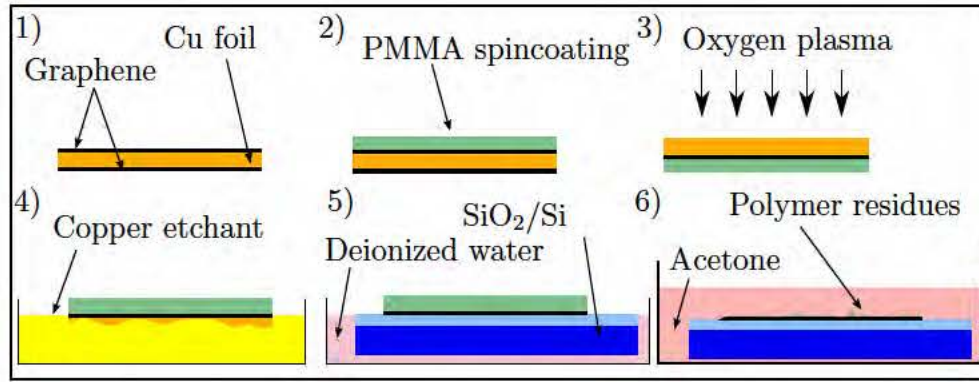


FIGURE 4.3: Schematic illustration of the graphene transfer process. 1) The Cu foil with graphene on both sides after the deposition, 2) PMMA layer spincoated on one side of the Cu foil, 3) graphene removed from bottom side of Cu foil by O_2 plasma treatment, 4) copper etching, 5) cleaning of the PMMA/Graphene membrane in deionized water and transfer to the target substrate, 6) removing of PMMA layer by acetone.

Next, the Cu foil is placed into the copper etching solution ($FeNO_3$, 0.05 g/ml). After sufficient amount of time (typically 12 hours), copper is completely etched away leaving the PMMA covered graphene on the surface of the etching solution.

PMMA/graphene structure is then transferred into deionized water to get rid of residues from the etching solution. This step is repeated several times.

In the following step, graphene is picked up from the deionized water by a target substrate, 280 nm thermal oxide on highly doped Si, and left to dry. The final step includes the removing PMMA supporting layer by cleaning in acetone, isopropyl alcohol and deionized water, respectively.

Contacts for electric connections of graphene with measuring electronic devices were manufactured by Electron Beam Lithography (EBL) (see section 4.2.2). Schematic illustration of this process is shown in Figure 4.4. In the process marked as 1) we start with graphene layer on SiO_2/Si substrate. PMMA pattern of a desired shape is formed by EBL. The whole sample is then exposed to oxygen plasma and uncovered graphene area is etched away. After this step, gold contacts are deposited by means of EBL and metal sputtering deposition.

Slightly different approach showed in Figure 4.4 as 2 differs from the first one in the order of steps. Graphene is transferred onto the substrate with pre-prepared gold contacts and following steps are then performed in the same order as in the case 1. The second process was preferentially used in experiments presented in this thesis.

Samples with prepared contacts were glued to the chip carriers. The connection between the gold contacts on the sample and the chip carriers was managed by ultrasonic welding of thin gold wire (wedge bonding) by the TPT HB16 wire bonder.

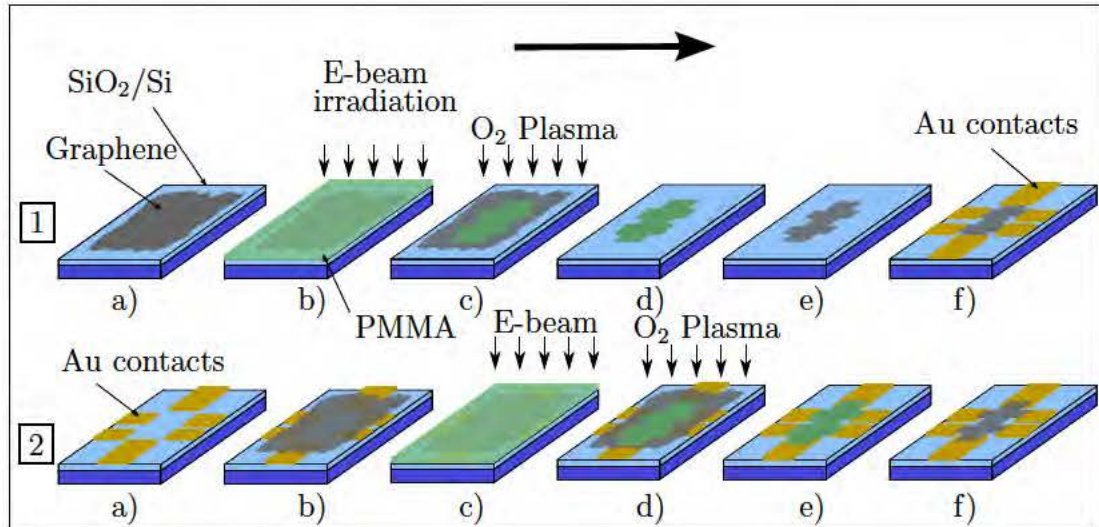


FIGURE 4.4: Schematic illustration of the contacting of graphene samples. Process 1: contacts are deposited after graphene is transferred on the sample. Process 2: Graphene is transferred on the sample with prepared contacts.

4.2 Scanning Electron Microscopy

Scanning electron microscopy is a technique using focused beam of electrons to produce magnified images of sample surface. Electrons emitted from a cathode are accelerated by high voltage (typically kilovolts) and focused on the sample. When electrons impinge on the surface, secondary electrons generated which can be registered by a detector. By scanning the beam over the sample and recording the signal from the detector, we obtain image containing the information about the intensity of detected secondary electron in each spot of the scanned area. Contrast on the image can be created either by topography of surface or by difference in emissivity of different materials.

Because the de Broglie wavelength of accelerated electrons is significantly smaller than the wavelength of light in visible spectrum scanning electron microscopes (SEM) can achieve good resolution at higher magnifications than optical microscopes limited by the light diffraction limit.

SEM images presented in Chapter 5 were produced by the instrument Tescan Lyra 3 XMH.

4.2.1 Energy Dispersive X-ray spectroscopy

Apart secondary electrons, other measurable signals are produced by the impact of accelerated electrons on the sample for example X-ray radiation. Spectrum of generated x-ray radiation has two parts. Continuous part of spectrum (Bremsstrahlung) is emitted by electrons losing its kinetic energy due to scattering by high electric field near the atom nuclei. Discrete part of the spectrum is also called characteristic X-ray radiation. When electrons from the inner shell are ejected from the electron shell by electrons from the beam, created vacancies are filled by electrons from higher energy shells. This process is related with emission

of Auger electron (irradiative transition) or X-ray photon (radiative transition) which energies are characteristic for each element.

The characteristic X-ray radiation is analyzed by Energy Dispersive X-ray spectroscopy (EDX). Photons are detected with semiconductor detector which produce current proportional to the energy of the photons. EDX is inbuilt inside the SEM microscope and this technique therefore allows to combine the standard SEM information with element analysis. EDX data presented in this thesis were obtained by Brooker X-ray analyzer coupled Tescan Lyra 3 SEM.

4.2.2 Electron Beam Lithography

Electron Beam Lithography (EBL) is a lithographic process used to create patterned structures by a focused electron beam.

Polymer layer (PMMA) evenly distributed on the substrate by spincoating. When parts of PMMA layer are irradiated by high dose of electrons, polymer chains are broken and these areas can be easily removed by a developer (MIBK:IPA solution). Patterned substrates can be used to metal deposition. When sample with deposited metal is placed into acetone bath, remaining polymer (unirradiated areas) with metal layer on top is removed and metal structures on irradiated parts stays on the sample (so called lift-off). Schematic illustration of this process can

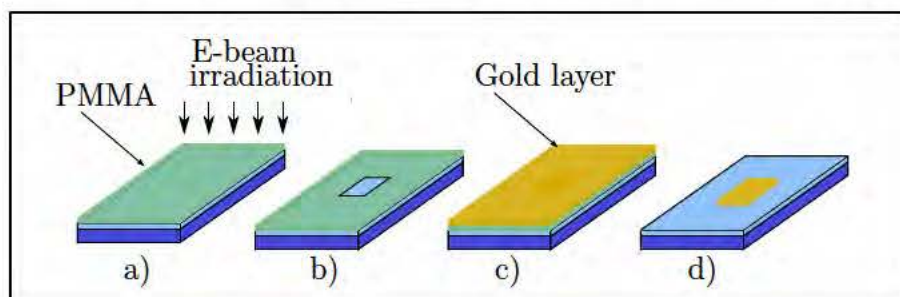


FIGURE 4.5: Schematics of the EBL procedure. a) Irradiation PMMA layer by electron beam, b) removing of the irradiated area by a developing agent, c) deposition of the gold layer, d) finished structure after the lift-off.

be found in Figure 4.5.

4.3 Raman Spectroscopy

Physical principle of Raman spectroscopy was explained in section 2.3. Raman measurements were performed with two different instruments at the Institute of Condensed Matter in Masaryk University in Brno. Standard measurements of spectra were performed by Raman spectroscopy Renishaw InVia with the He-Ne excitation laser of the wavelength 632.8 nm, power 50 mW and 2 μm spot size. The SPM NTegra Spectra + microRaman Solar III equipped with piezo scanning sample stage was used for mapping of Raman peak intensities. In this case, green excitation laser with wavelength 532 nm and power 0,8 mW was used and the spot size was approximately 0.5 μm .

4.4 Optical Microscopy

As it was mentioned earlier, the thickness of the substrate used for graphene layers is 280 nm. The reason for this is that this thickness supports constructive interference of multiple reflected incident light and allows the single layer graphene to be visible in optical microscope using white light illumination [77].

Optical images in this thesis were acquired by optical microscope Olympus MX51.

4.5 Atomic Force Microscopy

Atomic force microscopy (AFM) is a tool used for mapping a small-scale topography of surfaces. It uses a thin cantilever with a tip located at the end which scan over the surface. Interaction of the tip with the surface causes the change of the position of laser reflected from the cantilever which is measured by four-quadrant diode (see Figure 4.6). If we assign the displacement of the cantilever to the position of the tip in the plane of the sample we get a map of the topography of the sample surface.

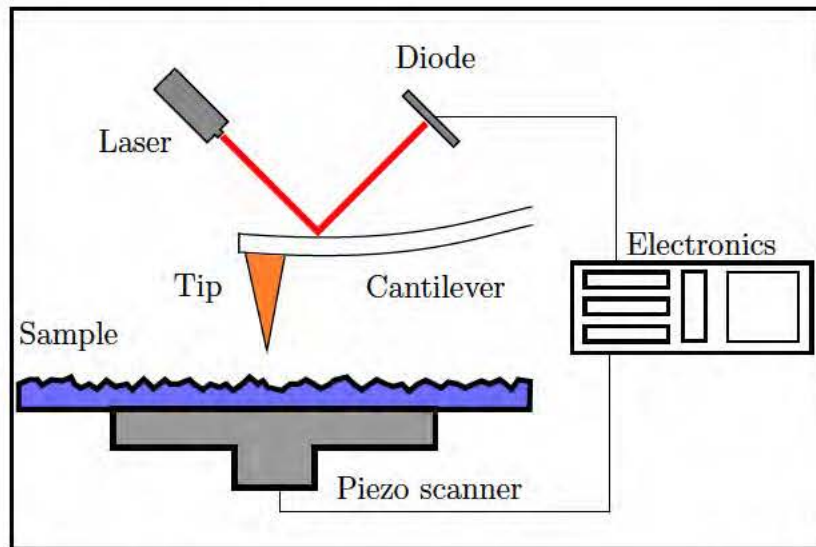


FIGURE 4.6: Schematic illustration of the Atomic Force Microscope

AFM can operate in two basic modes. In a contact mode, the tip directly touches the surface during the scanning. In a non-contact mode, the tip oscillates on its resonant frequency slightly above the surface and the signal is formed from the change of the resonant frequency.

AFM measurements were performed with the instrument SPM NT-MDT NTegra.

4.6 Electronic transport measurement

The setup for electronic transport measurements is shown in Figure 4.7 b). The excitation voltage (1 V – 5 V) is set via the lock-in amplifier (Stanford research

systems SR830). The signal goes through the $10\text{M}\Omega$ resistor, through the lock-in input and through the sample to the ground. The resistance of $10\text{ M}\Omega$ is much higher compared to the resistance of the sample so the set current (hundreds of nanoamperes) remains almost constant with changing sample resistance. Keithley 6221 current source provides the back-gate voltage by changing its compliance voltage in a circuit with $1\text{ M}\Omega$ resistor. Measurement parameters setting and data acquisition is performed via LabView interface.

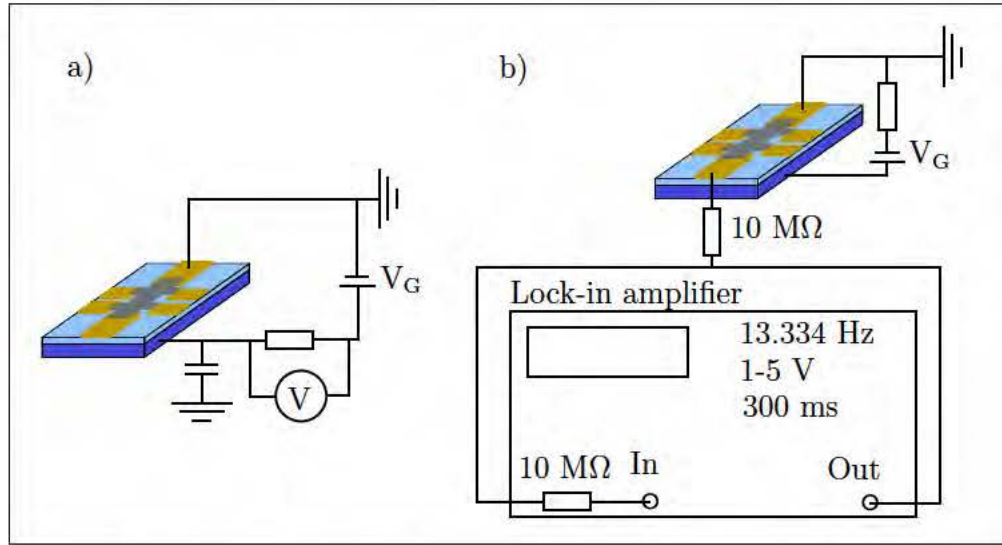


FIGURE 4.7: a) Electric scheme of the back-gate leakage current measurement, b) schematic of the electronic transport measurement with applied back-gate voltage. Lock-in frequency - 13.334 Hz, time constant 300 ms.

4.6.1 Electronic transport measurement in vacuum

Figure 4.8 a) shows the vacuum chamber used for the measurement of graphene samples at low pressures. The system is pumped by a turbomolecular pump and backing roots pump and the pressure is monitored by a cold cathode Penning gauge. The chip carrier is attached to the PBN heating element located on the manipulator (see Figure 4.8 b)). The heating element is heated by passing current and its temperature can be controlled by a K-type thermocouple.

The chamber was slightly modified to allow the electronic transport measurement. Six-pin electronic feedthrough was mounted to the port of the chamber. Pins for electric contacts on the chip carrier are connected to capton wires leading to the feedthrough connected to the measuring electronics by coaxial cables.

Chip carriers for vacuum measurement shown in Figure 4.8 c) were designed to fit the sample holder with the PBN heater. Chip carriers have six contacts with UHV compatible pins which one of them is permanently connected to the back-gate electrode and the others can be bonded to structures on the sample.

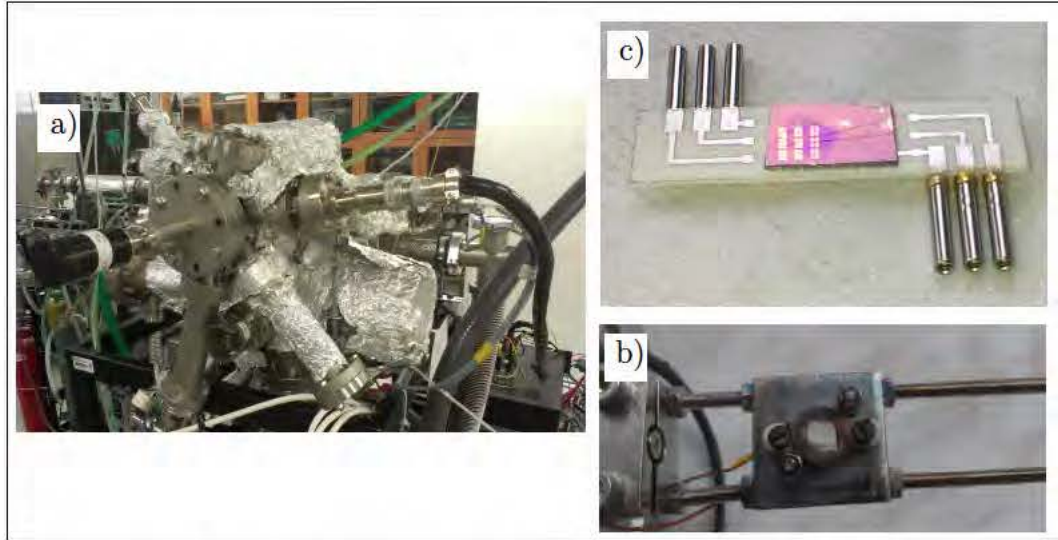


FIGURE 4.8: a) Vacuum chamber for electronic transport measurements, b) manipulator with the PBN sample holder, c) vacuum chip carrier.

4.6.1.1 Measurement of back-gate leakage current

Before the measurement of graphene device with applied gate voltage it is necessary to check the leakage current between the graphene structure and the back gate electrode. The setup for such measurement is shown in Figure 4.7 a). The voltage is applied between the gate electrode (bottom side of the silicon substrate) and a grounded graphene structure. When the voltage is increased (decreased) the capacitor starts to charge and one can measure a voltage drop on resistor due to the current flowing through. When the capacitor is charged, the current should decrease to zero. If there is a current leak between the gate electrode and graphene structure the current does not decrease after capacitor charging. This is the sign that it is not possible to use the device for measurements with applied gate voltage. In our experiments, we considered the leakage current negligible when the voltage drop on the resistor decrease below 1 mV at the back-gate voltage of 30 V.

During this work, leakage current was detected on several graphene devices but the direct cause was not identified. It was found that the bonding performed in the order from the chip carrier (1st bond) to the sample (2nd bond) and grounding of all contacts resulted in improvement but it did not solve the problem completely. Possible origins of damaging the SiO_2 layer could come from a thermal treatment of the sample, mechanical damaging and others. Therefore, more thorough investigation of this problem and optimization procedure of the sample preparation should be done in the future.

4.6.2 Low Temperature Measurement Setup

The instrument Quantum design Physical Property Measurement System EverCool II[®] (PPMSII) is capable of electronic transport measurements in temperature range 2 K – 400 K and in magnetic fields up to 9 T. In this case, samples were glued to spetial sample holders.

These measurements were performed at the Institute of Physics of Materials of the Academy of Sciences of the Czech Republic.

Chapter 5

Experimental Results

This chapter presents experimental results obtained in this work. The main focus of the thesis were the graphene single crystals which were studied by Raman spectroscopy, scanning electron microscopy and atomic force microscopy (section 5.1). Due to the effort to improve the quality of deposited graphene, the focus of the experimental work was changed to analysis of the impurities on the copper foil after the graphene growth (section 5.2). The contacting and measuring of the electronic transport properties of graphene were performed on polycrystalline graphene layers (section 5.3).

5.1 Graphene Single Crystals

Because of the contamination of the deposition system discovered later (see section 5.2), the series of experiments on the graphene single domain deposition were discontinued. This contamination very likely influences the mechanism of the graphene domain growth making any systematic study of the deposition unfeasible. Therefore, following two sections shows examples of the typical samples grown in our system analyzed by various methods.

5.1.1 Graphene single crystals on Cu foils

Graphene single crystals were deposited in the homebuilt CVD setup described in section 4.1.1. Figure 5.1 shows the first sample. The Cu foil (high purity, 25 μm thickness) was heated in a constant hydrogen flow of 3 sccm¹ at the pressure of 3 Pa (valve at 15%) to 1000 °C in 22 minutes. In the next step, the sample was exposed to the flow of methane (10 sccm) at the total pressure $p = 1 \cdot 10^1$ Pa for 5 minutes. Sample was then cooled down to the room temperature, exposed to the ambient atmosphere and removed from the furnace. Next, sample was heated on a hot plate at 200 °C for 10 minutes. The Cu foil covered with graphene (darker areas) is protected from oxidation whereas uncovered Cu areas (brighter areas) are strongly oxidized. This procedure was employed to increased the contrast between covered and uncovered Cu foil in the optical microscope.

¹standard cubic centimeter per minute

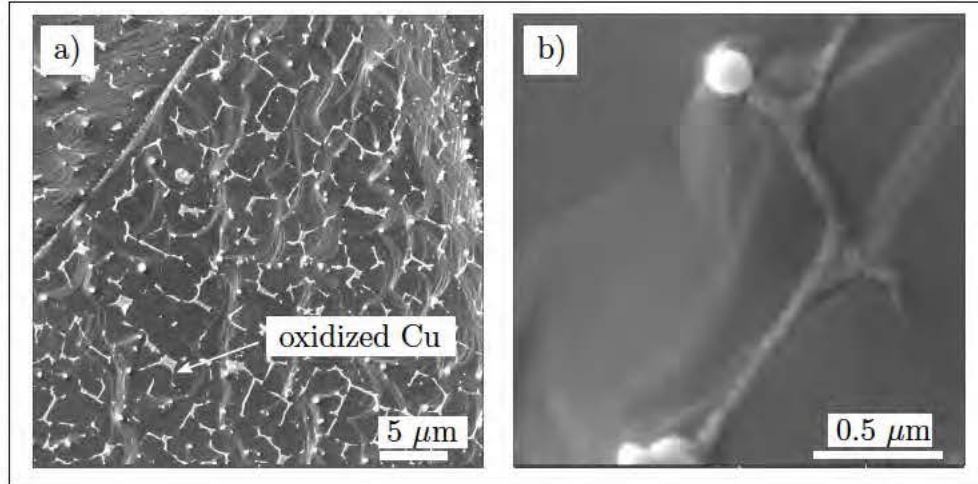


FIGURE 5.1: a) SEM image of the graphene deposited on the Cu foil graphene domains partially merged together - dark color, uncovered oxidized Cu foil - bright color, b) detail of the sample.

We can see that graphene domains are already merged together. Figure 5.2 shows a sample deposited under the same conditions but for a shorter deposition time (0.5 minute). Here we can recognize individual graphene domains separated by uncovered areas of the Cu foil. The size of domains can be roughly estimated as 5 μm but it varies over the whole sample.

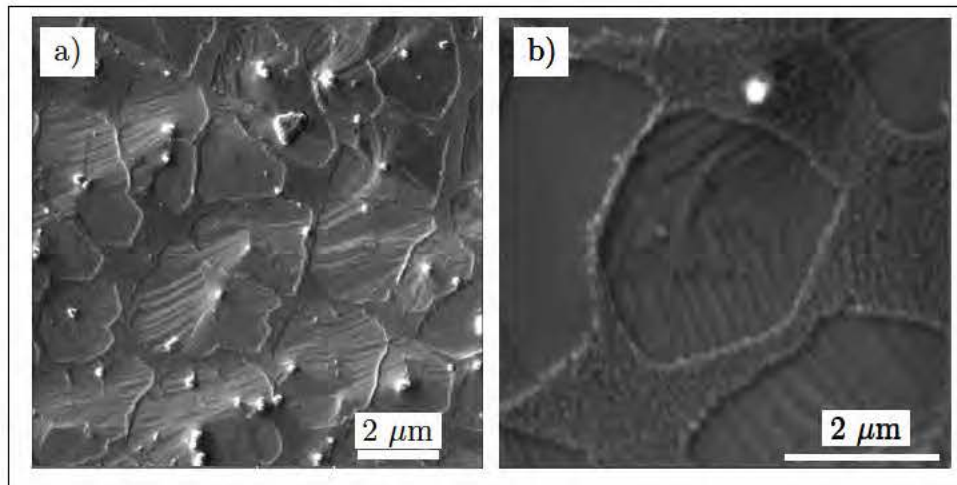


FIGURE 5.2: a) SEM image of the graphene deposited on the Cu foil. Isolated graphene domains, b) detail of the graphene domain.

The dependence of the domain sizes or the nucleation density on the deposition parameters (pressure, flow of gases) was not observed within other performed experiments (not presented here) and the results showed poor repeatability. In addition, high graphene grow rates and low deposition time needed to achieve isolated domains did not allow a precise control of the experimental conditions in our system.

Graphene samples grown by our procedure show irregular domain shapes. When a Cu foil was cooled down in a hydrogen flow (3 sccm, $p = 5 \cdot 10^0$ Pa)

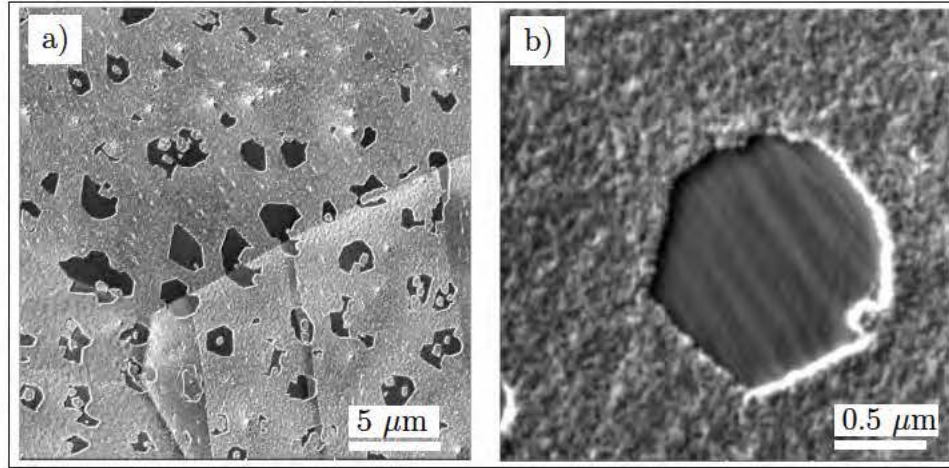


FIGURE 5.3: a) SEM image of the graphene deposited on the Cu foil and annealed in hydrogen after the deposition. Graphene domains shows more regular shapes then in the previous cases. b) Detail of the graphene domain.

after the deposition, etching of domains resulting in regular, almost hexagonal-like shapes was observed (see Figure 5.3). This could be assigned to the hydrogen induced graphene etching, where weaker graphene bonds are broken and domains posses more compact shapes as discussed in section 3.1.4.

Graphene domains were also found on the samples which were heated to 1000 °C without hydrogen flowing through the furnace. We can assume that in this case the the oxygen from native oxide layer on the Cu foil was not completely removed by the thermal decomposition during the annealing due to the absence of hydrogen. Remaining oxygen atoms can inhibit the nucleation of graphene [63] and could lead to larger graphene domains.

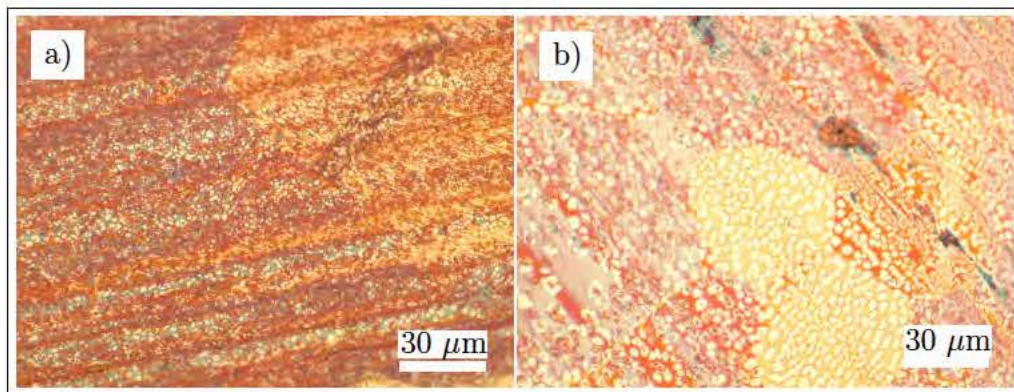


FIGURE 5.4: Optical microscope image of the graphene deposited on the Cu foil. a) Top side of the Cu foil, b) bottom side of the Cu foil.

Cu foils in these experiments were mounted on the sample holder by clamping to the molybdenum metal sheet (Figure 4.2). Although the main attention in the sample analysis was paid to the top side of the Cu foil, the results found on the bottom side of the foil also deserve to be mentioned.

In this case, the size of the graphene domains was significantly larger compared to the top side. This could be explained by comparing to similar sample

arrangements found in a literature. The specific feature of our setup is that the bottom side of the Cu foil is very close to the molybdenum sheet below. We can compare this to the case presented in the reference [70] where the Cu foil is folded into an envelope. Large graphene domains are found inside this envelope which Li et al. assigned to the redeposition of sublimated Cu atoms in the restricted volume. Despite the differences between our setup and the Cu foil envelope, we can assume that the mechanism of redeposition of sublimated Cu atoms could also be the origin of larger graphene domains observed in our experiments.

Other experiments in deposition of graphene single crystals were not performed due to impurities found on graphene grown on the Cu foil. The presence of impurities can significantly influence the character of graphene nucleation and damage the reliability of the obtained results.

5.1.2 Graphene single-crystals on SiO₂/Si

Graphene single-crystals grown on the Cu foil were transferred onto the SiO₂/Si samples. Figure 5.5 shows Raman analysis of small graphene domains ($\sim 1\mu\text{m}$). We can see from the intensity maps of 2D peak (Figure 5.5 b)) and G peak (Figure 5.5 c)) that sample consist of isolated graphene domains. Spectra in Figure 5.5 d) suggest that shown area consists of predominantly monolayer graphene.

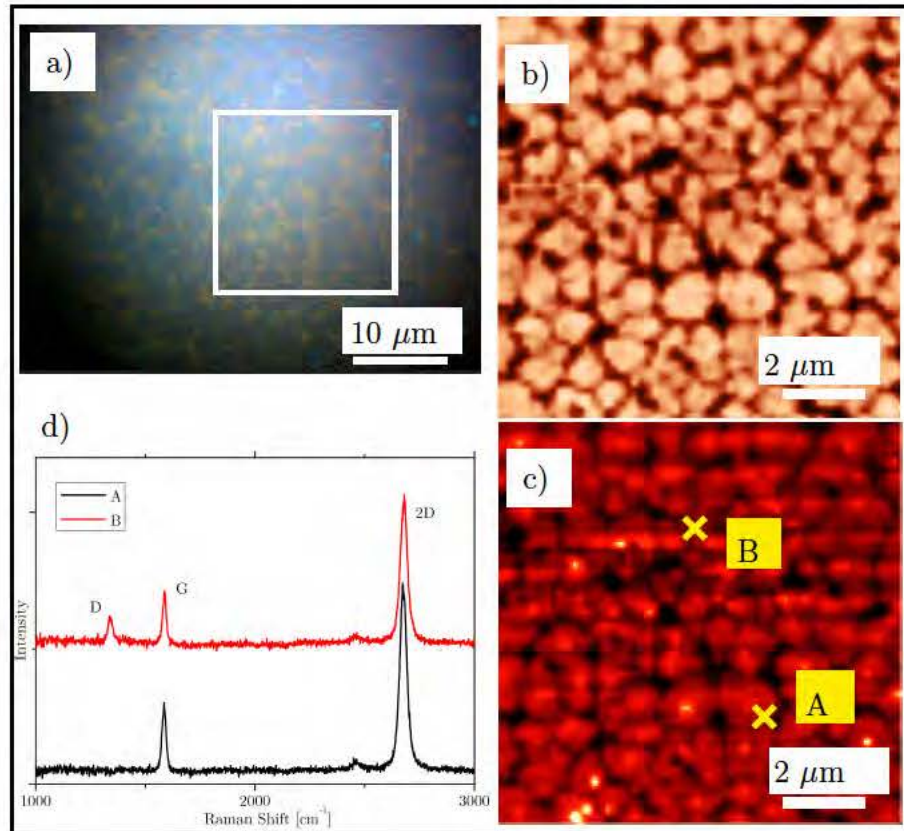


FIGURE 5.5: Raman analysis of small graphene domains. a) Optical image with marked mapped area, b) 2D peak intensity map, c) G peak intensity map, d) spectra extracted from the points A and B.

Raman analysis of large graphene domains transferred on the SiO_2/Si is presented in Figure 5.6. Darker areas in the middle of graphene domains in the optical microscope image reveal the second layer grown on the graphene monolayer. This is confirmed by comparison of the spectra (Figure 5.6 d)) taken from the darker area (the area close to the center of the domain, point B) and from the brighter area of the domain (point A). While the spectrum A shows the ratio of 2D and G peaks typical for single-layer graphene, spectrum B is typical for multilayer graphene, most probably double layer.

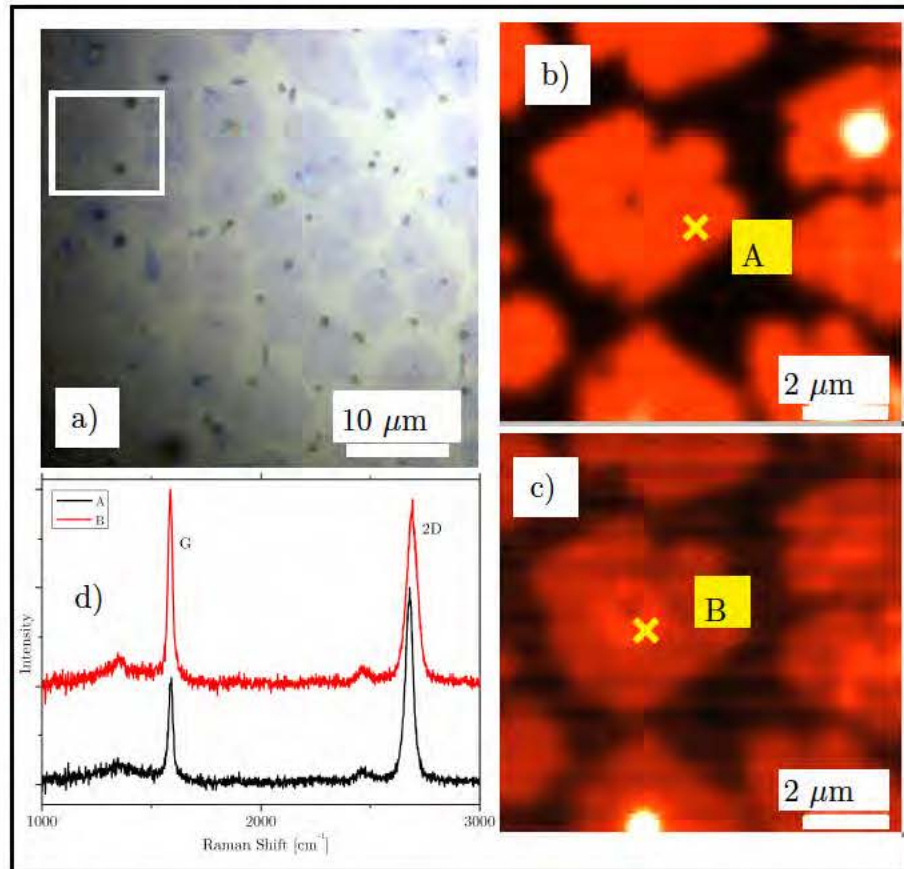


FIGURE 5.6: Raman analysis of large graphene domains. a) Optical image with marked mapped area, b) 2D peak map, c) G peak map, d) spectra extracted from the points A and B.

Various areas of the same sample were measured by SEM (5.7 a)) and AFM (5.7 b)). The central double layer area of graphene domains can be distinguished from the single layer areas in both of these images. Both images also show impurity particles present on the sample which can be most likely assigned to the PMMA residues.

5.2 Polycrystalline graphene and study of impurities

The motivation for detail examination of the surfaces of Cu foils after graphene deposition were defects observed on the Cu foil after the graphene growth. Graphene

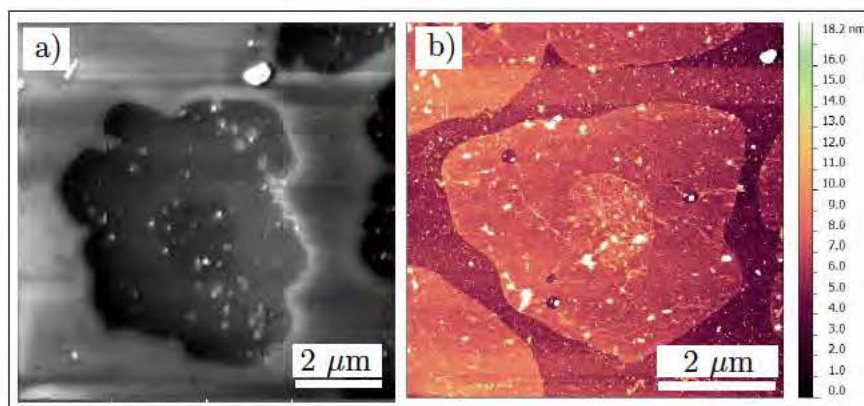


FIGURE 5.7: a) SEM image and b) AFM image of graphene domains.

was deposited on the Cu foils heated in hydrogen flow of 3sccm. Methane flow of 10 sccm was introduced to the furnace for 30 minutes.

Thorough SEM analysis of several samples showed various types of unwanted structures on our samples. Typical defects observed on more than one sample are depicted in Figure 5.8. In addition, several rare defects found on the samples are shown in Figure 5.9.

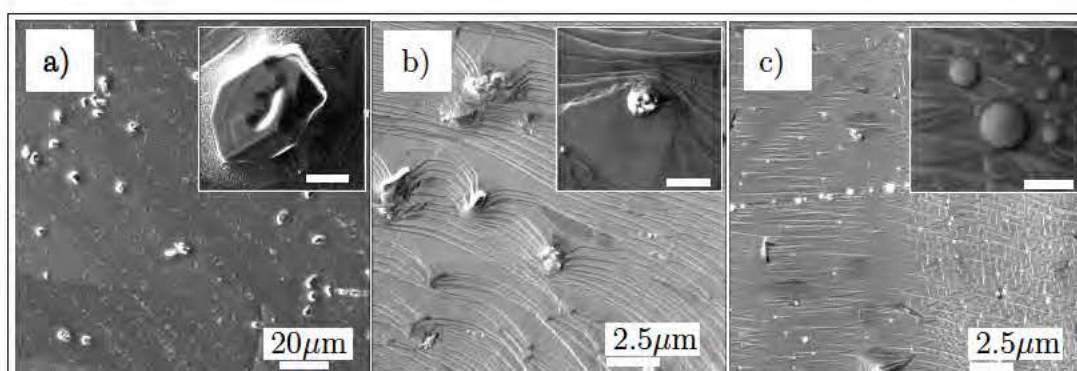


FIGURE 5.8: Typical defects found on the Cu foil. The scale bar of the inset is a) 1 μm b) 1 μm c) 0.5 μm .

All defects were studied by EDX analysis. We can see that spectra taken on dark crystalline structures from Figure 5.8 a) show strong signal of chromium and carbon (see Figure 5.10 d)). The map indicating the distribution of Cr and C peaks intensities is shown in Figure 5.10 b) and c).

Analysis of round shaped structures are shown in 5.11 b). The strongest signals in the spectrum were identified as silicon, oxygen and calcium. The third type of features consist from Fe, Cr, P and S (see Figure 5.11 a)).

According to the data presented above it was concluded that most probable cause for the presence of impurity defects (especially of those containing Fe and Cr) is the sample holder made mainly from stainless steel. In a context of these findings, the logical step was to remove the sample holder. Instead, the Cu foil was placed on a piece of quartz and thermocouple protected by the ceramic tube was placed directly on the inner surface of the quartz tube.

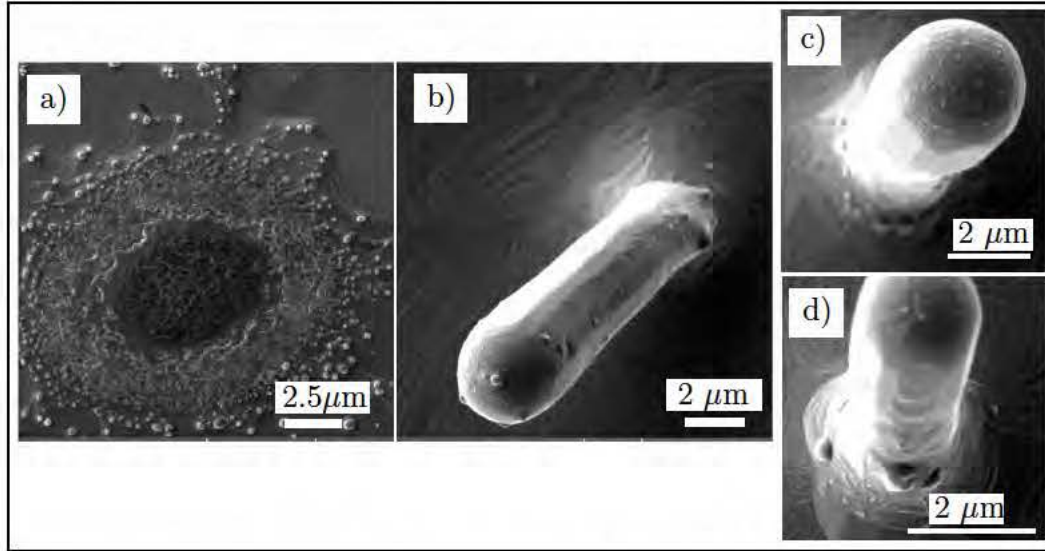


FIGURE 5.9: Non-typical defects found on the Cu foil.

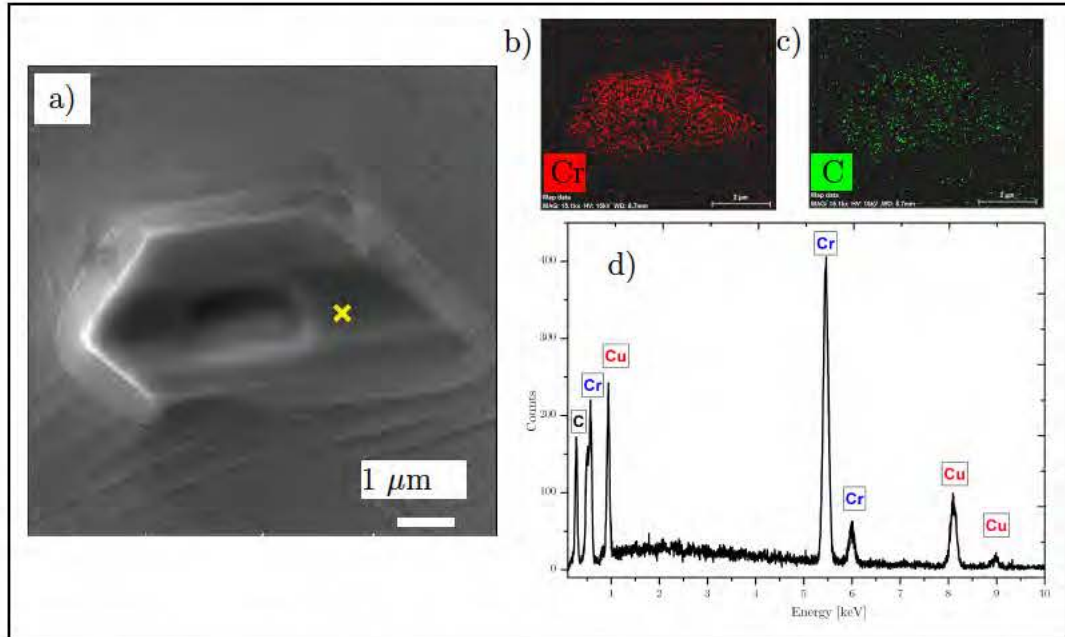


FIGURE 5.10: EDX analysis of defects found on Cu foil a) SEM image of analyzed area, b) chromium and b) carbon EDX map, d) EDX spectrum of taken from a point marked in a).

Figure 5.12 b) show the Cu foil after deposition by the new setup. Direct comparison of the Cu foil before and after the sample holder removal reveal striking improvement regarding the presence of impurities.

Although most of the defects on the Cu surface were eliminated, the round-shape type containing mainly silicon and oxygen can be found also with the new setup. Figure 5.13 shows the different area of the sample shown in 5.12 b). We can see that this side of the Cu foil was on higher temperature than the rest of it as we can assume from the melted edges.

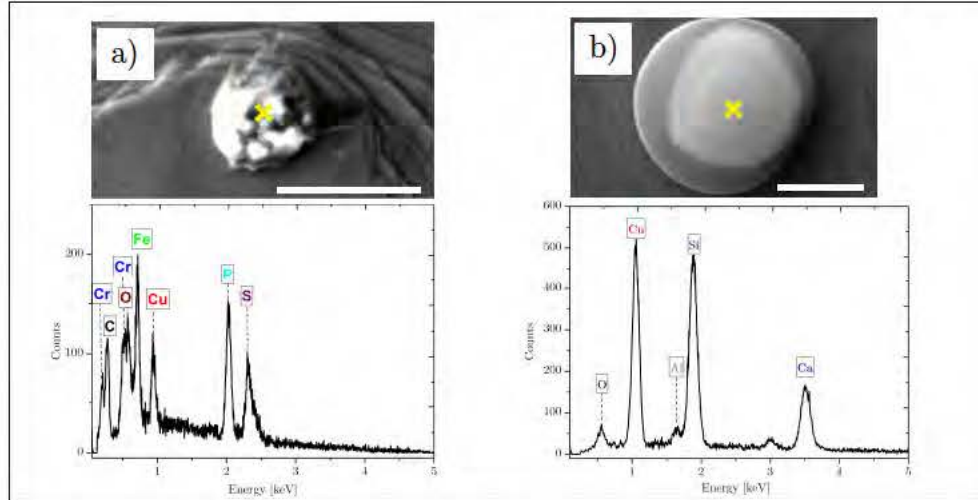


FIGURE 5.11: EDX analysis of defects found on the Cu foils. Scale bars of the images are a) 1 μm and b) 0.5 μm .

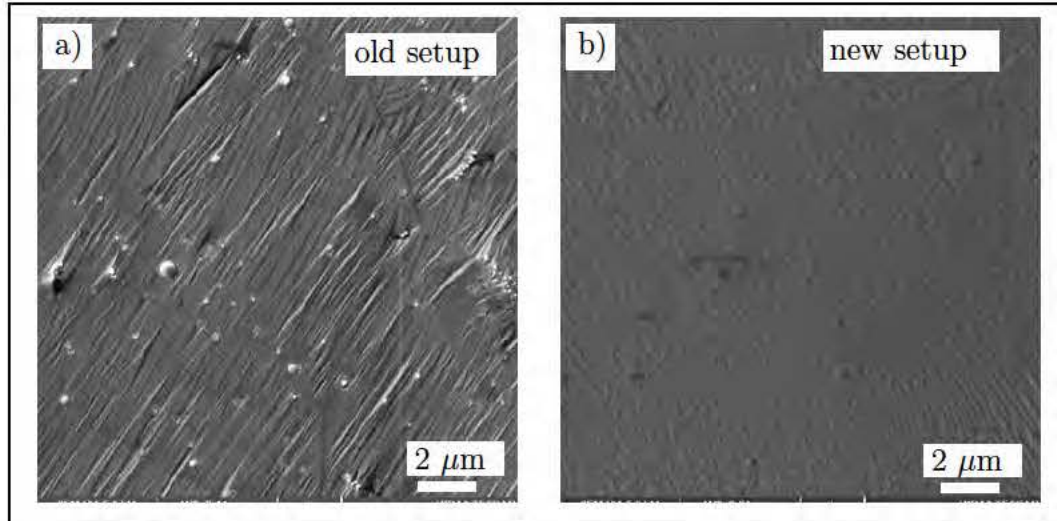


FIGURE 5.12: Comparison of the deposition with a) the old setup (with the metal sample holder) and b) the new setup (without the sample holder).

These features appeared also on samples prepared later and their origin remains unclear. One possibility is that they come from the quartz tube which could be locally overheated by the heating wire.

If this is the mechanism leading to the silicon oxide impurities the adjustment system would be necessary. The suggestion is that the heating wire should be set to not touch the the quartz tube directly as we can see in standard commercial deposition systems [78].

Unfortunately, oil contamination of the furnace components from their previous use can not be directly excluded although this possibility was considered to have low probability.

In addition, the inner surface of the quartz tube get covered with sooth at one point which suggests a non-standard behavior of the system. Full cleaning and required modifications of the system necessary to restore and improve deposition

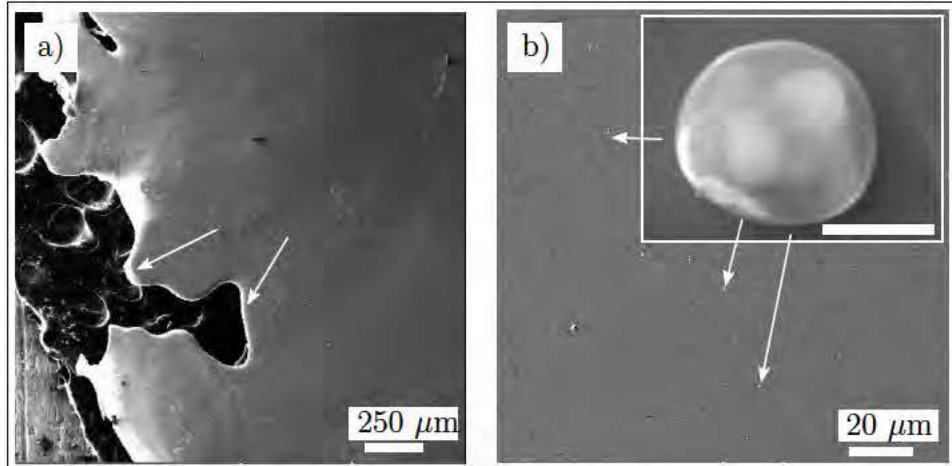


FIGURE 5.13: a) Melted edge of the Cu foil, b) Si defects found in the area near the melted (scale bar inset is 5 μm).

capabilities of the CVD furnace were not done during the time devoted to this thesis.

5.3 Electronic transport measurement

Electronic transport properties were measured on samples consisting from the polycrystalline graphene layer transferred onto the SiO_2/Si substrate with lithographically prepared gold contacts. The biggest complication in the sample preparation was the back-gate leakage current of the sample. Therefore, only few samples were possible to use in these measurements.

Presented samples were originally designed for the testing of the manufacturing procedure and the measurement setup and they do not have the typical shapes and dimensions employed for the electronic transport measurements.

5.3.1 Vacuum measurement of polycrystalline graphene

Measurements were performed according to the methods described in section 4.6.1. Data from the measurement of the sample 1 are summarized in Figure 5.14 a). The plot shows the dependence of the sample resistance on the applied gate voltage (back-gate trace). The arrangement of the contacts is shown in Figure 5.14 b). Used current was 500 nA.

The first measurement (black color in Figure 5.14) was done before the chamber was pumped. The second measurement (red color) was done at the chamber pressure $p = 4 \cdot 10^{-4}$ Pa. The sample was then annealed at 200 °C for 60 minutes and measured again (green color in Figure 5.14 a)). We can see only a small difference between the measurement in vacuum and at ambient conditions. The different values of the resistance from the first two cases and the measurement after annealing is more significant. Nevertheless, none of these curves shows a maximum which could be identified as a Dirac point.

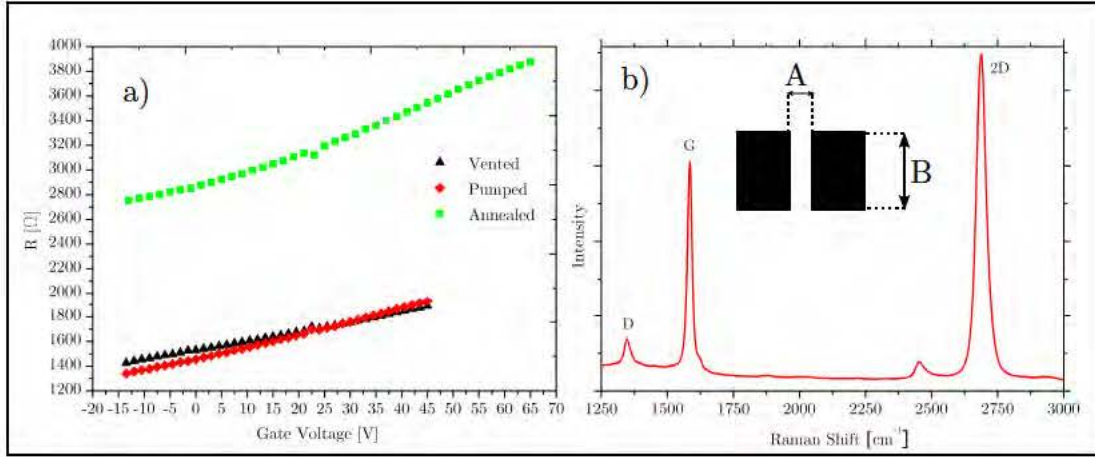


FIGURE 5.14: a) Dependence of the resistance of the sample on applied gate voltage. b) Raman spectra of the sample. The inset illustrates arrangement of sample electrodes. A=30 μm, B=200 μm.

At ambient conditions, adsorbents as air humidity or PMMA residues can cause doping of the graphene layer. This can induce shifting of the Dirac point towards higher (lower) gate voltages. Increasing sample resistance of the sample in Figure 5.14 indicates the hole doping of graphene. Dirac point is, in this case, shifted „far to the right”.

When the sample is annealed in vacuum, adsorbed water and impurities can desorb from the graphene layer and Dirac point is shifted closer to zero as observed, for example, in [21]. In our case, the annealing caused increase of the sample resistance, but the Dirac point was not observed up to the gate voltage of 65 V. This could be explained by doping of graphene by impurities which can not be easily removed by annealing. Raman spectra of the used sample is shown in Figure 5.14 b).

The data from Figure 5.14 a) can be used to estimate charge carrier mobilities (in this case the hole mobility) using parallel plate capacitor model [23]. Charge carrier concentration n in graphene layer induced by applied gate voltage V_G can be expressed as

$$n = \frac{\epsilon_0 \epsilon}{ed} V_G \quad (5.1)$$

where ϵ_0 is the vacuum permittivity, ϵ is the relative permittivity ($\epsilon_{\text{SiO}_2} = 3.9$), e is elementary charge and d is the thickness of the SiO_2 layer (300 nm).

The resistivity of the graphene layer is

$$\rho = R \frac{W}{L} = \frac{1}{\sigma} \quad (5.2)$$

where W is the sample width, L is the sample length and σ is the conductivity of the sample. Conductivity, according to Drude model, can be written as

$$\sigma = ne\mu \quad (5.3)$$

where μ stands for the charge carrier mobility. By combining equations (5.1) and (5.3), we get a relation

$$\sigma = \left(\frac{\epsilon_0 \epsilon}{d} \mu \right) V_G \quad (5.4)$$

where terms inside the bracket are constant. Therefore, the charge carrier mobility can be estimated from the slope of the function expressed by (5.4). The results for the presented sample are shown in Figure 5.15.

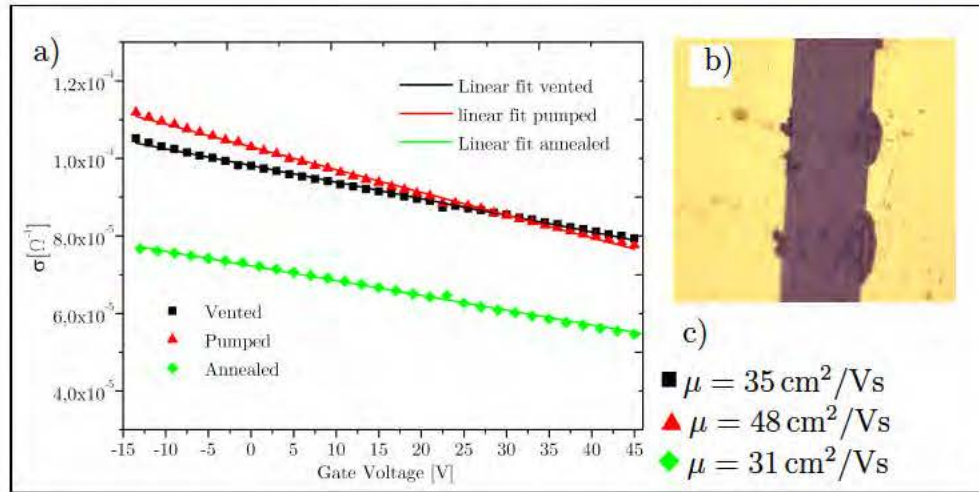


FIGURE 5.15: a) Dependence of the conductivity of the sample on applied gate voltage, b) optical microscope image of the structure, c) hole mobilities corresponding to curves from a).

We can see, that highest charge carrier mobility is found for the sample in vacuum before the annealing and the lowest mobility corresponds to the sample measured at ambient conditions. The annealing of the sample probably caused degradation of the graphene layer which could cause slightly lower mobility. Nevertheless, mobilities of presented sample are significantly lower than values typically reported for graphene prepared by CVD on SiO_2 substrate by wet transfer ($500 \text{ cm}^2/\text{Vs}$ – $10000 \text{ cm}^2/\text{Vs}$ [48]). The reason for this can be highly defected and contaminated graphene (see Chapter 4) or the transfer and cleaning processes induced sample degradation.

The sample 2 consisted from the same lithographically prepared gold electrodes as the sample 1. The distance between the electrodes was, in this case, $50 \mu\text{m}$. The first measurement of the back-gate trace was performed at the ambient atmosphere (black color in Figure 5.16). Calculated mobility of the sample was $605 \text{ cm}^2/\text{Vs}$ which was the highest value from all of our samples. Next, the sample was introduced into the vacuum chamber. It was annealed for 2 hours at 150°C at a pressure $5 \cdot 10^{-3} \text{ Pa}$. After the annealing, the sample was exposed to the ambient atmosphere and measured again (red color in Figure 5.16). We can see that the mobility of the sample is approximately two times lower than before the annealing. The decrease of the mobility after the annealing is qualitatively in agreement with the measurement of the sample 1.

The last measured sample was the sample 3. The distance of the electrodes was $50 \mu\text{m}$. The results of the measurements are shown in Figure 5.17. The

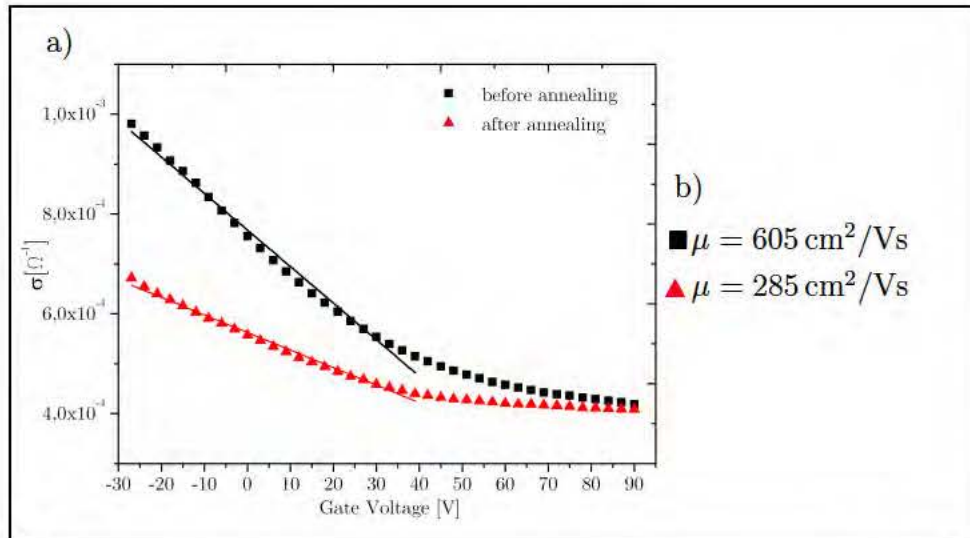


FIGURE 5.16: a) Dependence of the conductivity of the sample 2 on applied gate voltage, b) mobilities calculated from the slope of the fitted lines.

sample was measured first at the ambient atmosphere (black squares). The second measurement (red circles) was done after the chamber was pumped to the pressure $p = 1 \cdot 10^{-4}$ Pa. For the first time in our experiments, we observed the minimum of the conductivity curve - the Dirac point - located at 57 V of the back-gate voltage². We can also see a slight increase in mobility of the sample compared to the measurement at ambient atmosphere. Next, the sample was annealed at 150 °C for 0.5, 2 and 3 hours, consequently. The sample was cooled down and measured after each of these annealing steps. We can see, that the mobility of the sample reached a lower values almost after every annealing³.

The slope of the curves on the right of the Dirac point relates to the mobility of electrons. We can see that the slope is much lower than in the case of holes.

The position of the Dirac point is influenced by the annealing. It is shifted from 57 V to 52 after the third measurement (green triangles). The fourth measurement (blue diamonds) shows the position of the Dirac point at 23 V. After the last annealing step (orange triangles), the Dirac point was shifted towards the higher voltage values at 37 V. The shifting of the Dirac point and changes in the mobility of the sample are very likely connected with the desorption of molecules absorbed on the graphene surface including polymer residues from the transition process.

The last measurement of the sample 3 was done after the exposure of the sample to the ambient atmosphere (see Figure 5.18). The position of the Dirac point before the venting of the chamber was 37 V. Immediately after the venting, the Dirac point was found at 25 V. Its position was found at 36 V after 20 minutes

²Presented values of the Dirac point positions were estimated from the minimum (maximum) of the conductivity (resistance) curves.

³The mobilities were calculated from the fitted lines which are not shown in the Figure. Lines were fitted in the range of -30 V–50 V for the first measurement, -60 V–50 V for the second, -60 V–40 V for the third, -30 V–20 V for the fourth and -60 V–35 V for the fifth.

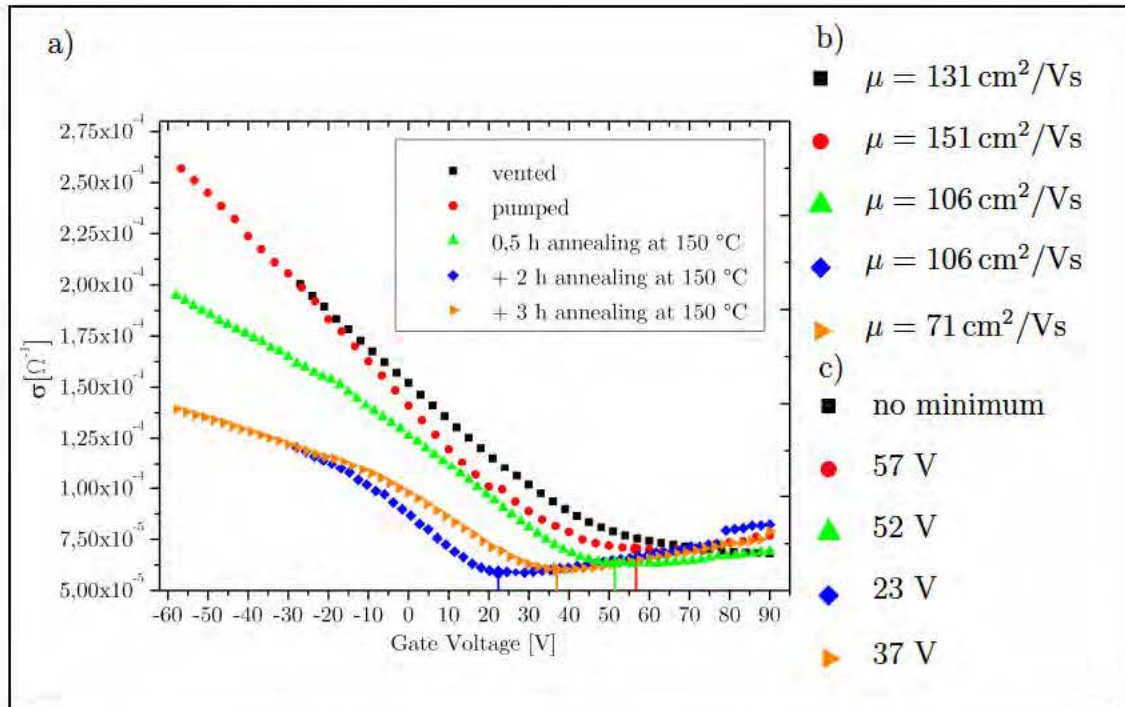


FIGURE 5.17: a) Dependence of the conductivity of the sample 3 on applied gate voltage for several annealing times, b) calculated mobilities, c) positions of the Dirac point.

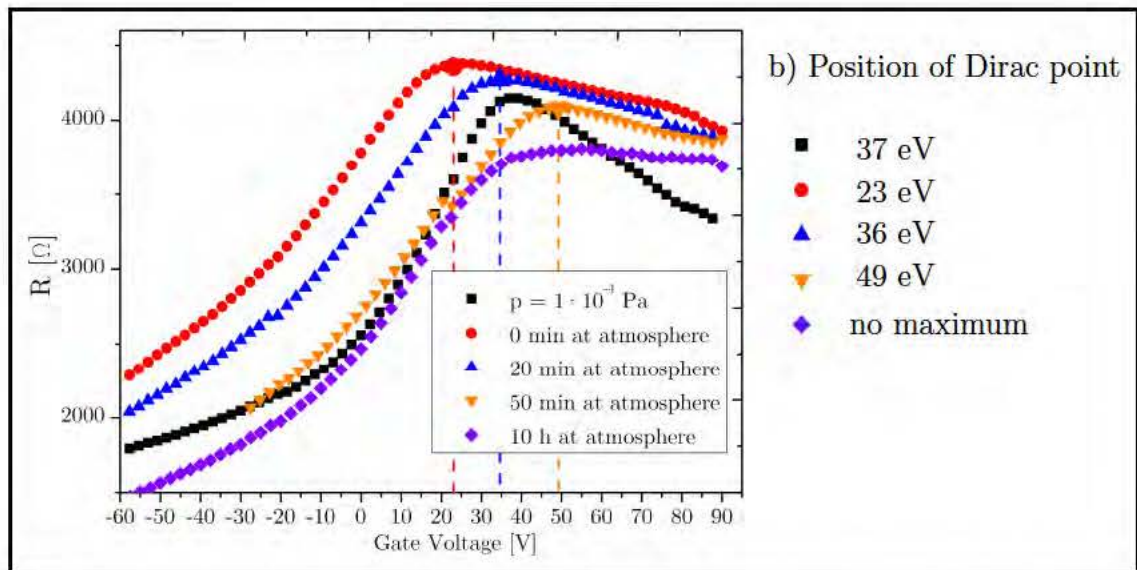


FIGURE 5.18: a) Dependence of the resistance of the sample 3 on applied gate voltage after exposure of the sample to ambient atmosphere, b) positions of the Dirac point.

and at 49 V after 50 minutes at the ambient atmosphere. After 10 hours at ambient atmosphere, the position of the Dirac point was not possible to determine.

5.3.2 Low Temperature and Magnetic field Measurement

The setup for the low temperature measurement is described in section 4.6.2. For this experiments, we used polycrystalline graphene layer contacted by electrodes shown in the inset of Figure 5.19 b). After the sample was introduced into the apparatus, the system was pumped to the pressure $\sim 3 \cdot 10^{-1}$ Pa. Next, the sample was heated up to the temperature 395 K (~ 122 °C) and left at this temperature for 20 minutes (see Figure 5.19 a)). Afterwards, the sample was cooled down to the room temperature. The resistance of the sample is lower after the annealing probably due to the desorption of adsorbed molecules possibly acting as scattering centers for charge carriers. Figure 5.19 b) shows Raman spectrum of the sample and a geometry of electrodes ($B=400$ μm , $A=50$ μm).

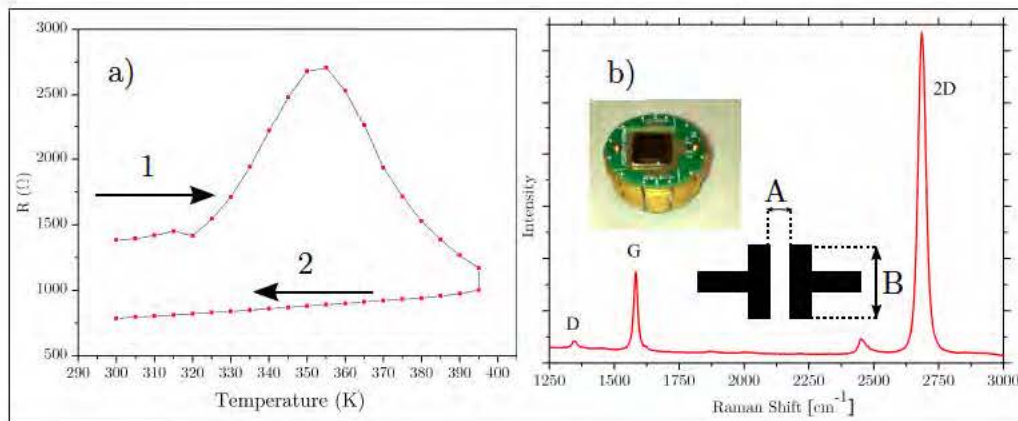


FIGURE 5.19: a) Initial annealing of the sample in low temperature measurement setup, numbers and arrows mark the order of the process, b) Raman spectra of the sample, the inset shows sample in the sample holder and the geometry of the electrodes ($B=400$ μm , $A=50$ μm).

The sample was then cooled to 2 K and heated back to the room temperature. The resistance of the sample increases with decreasing temperature as is shown in Figure 5.20 a).

The last measurement is related to the dependence of the sample resistance on a magnetic field applied perpendicularly to the surface of the sample. The part of sample with a distance of the electrodes $B = 400$ μm , $A = 200$ μm was employed in this experiment. The temperature of the sample was kept at 2 K and the applied magnetic field was in the range of 0 T – 9 T. The result shown in Figure 5.20 exhibits Shubnikov-de Haas oscillations (see section 2.2).

Due to the leakage current between the back-gate electrode and graphene layer, this sample could not be involved in transport measurements with applied gate voltage which would allow to determine the position of the Dirac point. The position of the Dirac point can be derived from the values of minima in SdH oscillations as it was done for our sample in [79]. The calculated position of the Dirac point was estimated to be 13.6 V.

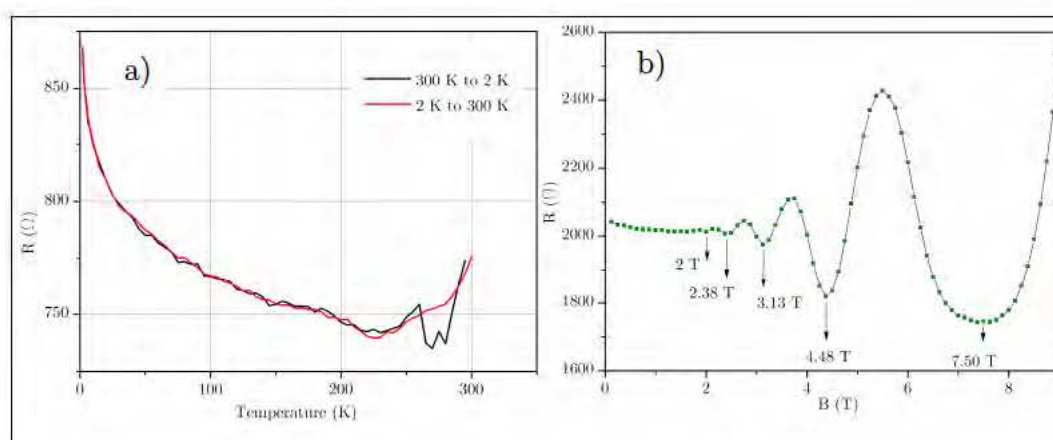


FIGURE 5.20: a) Cooling and heating of the graphene sample to 2 K and back to the room temperature, b) Dependence of the sample resistivity on magnetic field perpendicular to the sample surface.

Chapter 6

Conclusion

This thesis deals with the chemical vapor deposition of graphene. Chapter 2 is focused on the fundamental properties of graphene with an emphasis on electronic transport properties, quantum Hall effect and Raman spectra interpretation.

Chemical vapor deposition of graphene on copper is reviewed in Chapter 3. It presents the basic processes taking place on the Cu foil during CVD and discusses the influence of deposition parameters.

Chapter 4 describes experimental methods and setups used for preparation and analysis of the samples.

Chapter 5 contains obtained experimental results. The first part of the experiments is focused on the deposition of graphene single crystals. Graphene domains grown on the Cu foil are characterized by optical and electron microscopy. The graphene samples were then transferred onto Si/SiO₂ and studied by Raman spectroscopy and atomic force microscopy. The next part of the chapter presents analysis of defects found on the Cu foil after graphene deposition by energy dispersive X-ray spectroscopy. The amount of impurities found on the Cu foil was reduced by removing the metal sample holder from the deposition system. The impurities containing silicon were still found on the sample in the new setup. It was suggested that the reason for the presence of this impurities might be related to the construction of the homebuilt CVD furnace.

The last section of Chapter 5 shows the results of the electronic transport measurement of graphene polycrystalline layers. The major problem of this part was the back-gate leakage current observed for many samples. This fact did not allow us to measure more samples with the applied gate voltage. We observed the Dirac point for one of the samples measured in vacuum. We were able to measure the change of its position caused by the annealing or the exposure to the atmosphere. The results from the measurement of the back-gate trace of the sample with increasing time of the exposure to the ambient atmosphere could be interesting in a context of the graphene application as a humidity sensor which is one of the main research topics in the graphene group at the Institute of Physical Engineering.

The vacuum chamber prepared for purpose of the electronic-transport measurements in this thesis could be easily modified for the experiments investigating the response of the graphene devices on, for example, gas introduced into the

vacuum chamber or the material deposited on graphene.

One of our samples was measured at low temperatures with the magnetic field applied perpendicularly to the sample surface. We observed Shubnikov-de Haas oscillations proving the presence of a two-dimensional electron system represented by the graphene layer. This is an interesting result if we take into account the contamination of the CVD system and PMMA residues on the surface of our samples.

The author believes that the outcomes of the thesis, especially those connected with the graphene CVD synthesis, will help to improve the quality of graphene samples prepared at the Institute of Physical Engineering.

Bibliography

- [1] Novoselov, K. S., Geim, A. K., Morozov, S. V., Jiang, D., Zhang, Y., Dubonos, S. V., Grigorieva, I. V., and Firsov, A. A. Electric field effect in atomically thin carbon films. *Science*, 306 (5696), **2004**, pp. 666–669.
- [2] Novoselov, K. S., Fal’ko, V. I., Colombo, L., Gellert, P. R., Schwab, M. G., and Kim, K. A roadmap for graphene. *Nature*, 490 (7419), **2012**, pp. 192–200.
- [3] Nobel Media AB 2013. *The Nobel Prize in Physics 2010*, 2014. Available on-line: http://www.nobelprize.org/nobel_prizes/physics/laureates/2010/.
- [4] Lin, Y.-M., Dimitrakopoulos, C., Jenkins, K. a., Farmer, D. B., Chiu, H.-Y., Grill, A., and Avouris, P. 100-GHz transistors from wafer-scale epitaxial graphene. *Science (New York, NY)*, 327 (5966), **2010**, pp. 662–662.
- [5] Wang, X., Zhi, L., and Müllen, K. Transparent, conductive graphene electrodes for dye-sensitized solar cells. *Nano letters*, 8 (1), **2008**, pp. 323–7.
- [6] Wu, J., Agrawal, M., Becerril, H., Bao, Z., and Liu, Z. Organic light-emitting diodes on solution-processed graphene transparent electrodes. *ACS Nano*, 4 (1), **2009**, pp. 43–48.
- [7] Kim, K. S., Zhao, Y., Jang, H., Lee, S. Y., Kim, J. M., Kim, K. S., Ahn, J.-H., Kim, P., Choi, J.-Y., and Hong, B. H. Large-scale pattern growth of graphene films for stretchable transparent electrodes. *Nature*, 457 (7230), **2009**, pp. 706–10.
- [8] Schedin, F., Geim, A. K., Morozov, S. V., Hill, E. W., Blake, P., Katsnelson, M. I., and Novoselov, K. S. Detection of individual gas molecules adsorbed on graphene. *Nature materials*, 6 (9), **2007**, pp. 652–655.
- [9] Zhang, H., Lv, X., Li, Y., Wang, Y., and Li, J. P25-graphene composite as a high performance photocatalyst. *ACS nano*, 4 (1), **2010**, pp. 380–386.
- [10] Huang, X., Qi, X., Boey, F., and Zhang, H. Graphene-based composites. *Chemical Society reviews*, 41 (2), **2012**, pp. 666–86.
- [11] Chung, C., Kim, Y., and Shin, D. Biomedical applications of graphene and graphene oxide. *Accounts of chemical research*, 46 (10), **2013**, pp. 2211–2224.
- [12] Postma, H. W. C. Rapid sequencing of individual DNA molecules in graphene nanogaps. *Nano letters*, 10 (2), **2010**, pp. 420–5.
- [13] Bae, S., Kim, H., Lee, Y., Xu, X., Park, J.-S., Zheng, Y., Balakrishnan, J., Lei, T., Kim, H. R., Song, Y. I., Kim, Y.-J., Kim, K. S., Ozyilmaz, B., Ahn, J.-H., Hong, B. H., and Iijima, S. Roll-to-roll production of 30-inch graphene films for transparent electrodes. *Nature nanotechnology*, 5 (8), **2010**, pp. 574–8.

- [14] Castro Neto, A., Peres, N., Novoselov, K. S., and Geim, A. Electronic properties of graphene nanostructures. *Reviews of Modern Physics*, 81, **2009**, pp. 109–162.
- [15] Geim, A. K. and Novoselov, K. S. The rise of graphene. *Nature materials*, 6 (3), **2007**, pp. 183–91.
- [16] Meyer, J., Geim, A., and Katsnelson, M. The structure of suspended graphene sheets. *Nature*, 446, **2007**, pp. 60–63.
- [17] Cooper, D. R., D’Anjou, B. B., Ghattamaneni, N., Harack, B., Hilke, M., Horth, A., Majlis, N., Massicotte, M., Vandsburger, L., Whiteway, E., and Yu, V. Experimental review of graphene. *ISRN Condensed Matter Physics*, 2012, **2012**.
- [18] Nagashio, K. and Yamashita, T. Electrical transport properties of graphene on SiO₂ with specific surface structures. *Journal of Applied Physics*, , **2011**, pp. 1–9.
- [19] Ren, Y., Chen, S., Cai, W., Zhu, Y., Zhu, C., and Ruoff, R. S. Controlling the electrical transport properties of graphene by in situ metal deposition. *Applied Physics Letters*, 97 (5), **2010**, p. 053107.
- [20] Song, H. S., Li, S. L., Miyazaki, H., Sato, S., Hayashi, K., Yamada, a., Yokoyama, N., and Tsukagoshi, K. Origin of the relatively low transport mobility of graphene grown through chemical vapor deposition. *Scientific reports*, 2, **2012**.
- [21] Chen, S., Cai, W., Chen, D., Ren, Y., Li, X., Zhu, Y., Kang, J., and Ruoff, R. S. Adsorption/desorption and electrically controlled flipping of ammonia molecules on graphene. *New Journal of Physics*, 12 (12), **2010**, p. 125011.
- [22] Nobel Media AB 2013. *The Nobel Prize in Physics 1985*, 2014. Available on-line: http://www.nobelprize.org/nobel_prizes/physics/laureates/1985/press.html.
- [23] Ihn, T. *Semiconductor Nanostructures: Quantum States and Electronic Transport*. OUP Oxford, 2010. ISBN 9780199534432.
- [24] Wei, H. P., Lin, S. Y., and Tsui, D. Effect of long-range potential fluctuations on scaling in the integer quantum Hall effect. *Physical Review B*, 45 (7), **1992**, p. 3926.
- [25] Zhang, Y., Tan, Y.-w., Stormer, H. L., and Kim, P. Experimental observation of the quantum Hall effect and Berry’s phase in graphene. *Nature*, 438, **2005**, pp. 201–204.
- [26] Novoselov, K., McCann, E., and Morozov, S. Unconventional quantum Hall effect and Berry’s phase of 2π in bilayer graphene. *Nature Physics*, 2, **2006**, pp. 177–170.
- [27] Novoselov, K. S., Jiang, Z., Zhang, Y., Morozov, S. V., Stormer, H. L., Zeitler, U., Maan, J. C., Boebinger, G. S., Kim, P., and Geim, a. K. Room-temperature quantum Hall effect in graphene. *Science (New York, NY)*, 315 (5817), **2007**, pp. 1379–1379.
- [28] Ferrari, A. Raman spectroscopy of graphene and graphite: disorder, electron–phonon coupling, doping and nonadiabatic effects. *Solid State Communications*, 143, **2007**, pp. 47–57.

- [29] Dimiev, A., Kosynkin, D. V., Sinitskii, A., Slesarev, A., Sun, Z., and Tour, J. M. Layer-by-layer removal of graphene for device patterning. *Science*, 331 (6021), **2011**, pp. 1168–1172.
- [30] Geim, A. K. Graphene: status and prospects. *Science*, 324 (5934), **2009**, pp. 1530–1534.
- [31] Dreyer, D. R., Ruoff, R. S., and Bielawski, C. W. From conception to realization: an historical account of graphene and some perspectives for its future. *Angewandte Chemie (International ed in English)*, 49 (49), **2010**, pp. 9336–44.
- [32] Song, W., Jeon, C., Youn Kim, S., Kim, Y., Hwan Kim, S., Lee, S.-I., Jung, D. S., Jung, M. W., An, K.-S., and Park, C.-Y. Two selective growth modes for graphene on a Cu substrate using thermal chemical vapor deposition. *Carbon*, 68, **2014**, pp. 87–94.
- [33] Celebi, K., Cole, M. T., Teo, K. B. K., and Park, H. G. Observations of Early Stage Graphene Growth on Copper. *Electrochemical and Solid-State Letters*, 15 (1), **2012**, pp. K1–K4.
- [34] Zhang, B., Lee, W. H., Piner, R., Kholmanov, I., Wu, Y., Li, H., Ji, H., and Ruoff, R. S. Low-temperature chemical vapor deposition growth of graphene from toluene on electropolished copper foils. *ACS nano*, 6 (3), **2012**, pp. 2471–2476.
- [35] Yan, Z., Lin, J., Peng, Z., Sun, Z., Zhu, Y., Li, L., Xiang, C., Loi, E., Kittrell, C., and Tour, J. M. Toward the Synthesis of Wafer-Scale Single-Crystal Graphene on Copper Foils. *ACS nano*, 6 (10), **2012**, pp. 9110–9117.
- [36] Muradov, N. and Vezirolu, T. From hydrocarbon to hydrogen? Carbon to hydrogen economy. *International Journal of Hydrogen Energy*, 30 (3), **2005**, pp. 225–237.
- [37] Fulcheri, L. and Schwob, Y. From Methane to Hydrogen, Carbon and Water. *International Journal of Hydrogen Energy*, 20 (3), **1995**, pp. 197–202.
- [38] Sun, J., Cole, M. T., Lindvall, N., Teo, K. B. K., and Yurgens, A. Noncatalytic chemical vapor deposition of graphene on high-temperature substrates for transparent electrodes. *Applied Physics Letters*, 100 (2), **2012**, p. 022102.
- [39] Mattevi, C., Kim, H., and Chhowalla, M. A review of chemical vapour deposition of graphene on copper. *Journal of Materials Chemistry*, 21 (10), **2011**, pp. 3324–3334.
- [40] Edwards, R. S. and Coleman, K. S. Graphene film growth on polycrystalline metals. *Accounts of chemical research*, 46 (1), **2013**, pp. 23–30.
- [41] Yu, Q., Lian, J., Siriponglert, S., Li, H., Chen, Y. P., and Pei, S.-S. Graphene segregated on Ni surfaces and transferred to insulators. *Applied Physics Letters*, 93 (11), **2008**, p. 113103.
- [42] Zhang, Y., Zhang, L., and Zhou, C. Review of chemical vapor deposition of graphene and related applications. *Accounts of chemical research*, , **2013**, pp. 2329–2339.
- [43] Ago, H., Ogawa, Y., Tsuji, M., Mizuno, S., and Hibino, H. Catalytic Growth of Graphene: Toward Large-Area Single-Crystalline Graphene. *The Journal of Physical Chemistry Letters*, 3 (16), **2012**, pp. 2228–2236.

- [44] Kim, H., Mattevi, C., Calvo, M. R., Oberg, J. C., Artiglia, L., Agnoli, S., Hirjibehedin, C. F., Chhowalla, M., and Saiz, E. Activation energy paths for graphene nucleation and growth on Cu. *ACS nano*, 6 (4), **2012**, pp. 3614–23.
- [45] Seah, C.-M., Chai, S.-P., and Mohamed, A. R. Mechanisms of graphene growth by chemical vapour deposition on transition metals. *Carbon*, 70, **2014**.
- [46] Vlassiounk, I., Smirnov, S., Regmi, M., Surwade, S. P., Srivastava, N., Feenstra, R., Eres, G., Parish, C., Lavrik, N., Datskos, P., Dai, S., and Fulvio, P. Graphene Nucleation Density on Copper: Fundamental Role of Background Pressure. *The Journal of Physical Chemistry C*, 117 (37), **2013**, pp. 18919–18926.
- [47] Jauregui, L., Cao, H., Wu, W., Yu, Q., and Chen, Y. Electronic properties of grains and grain boundaries in graphene grown by chemical vapor deposition. *Solid State Communications*, 4 (151), **2011**, pp. 1100–1104.
- [48] Petrone, N., Dean, C. R., Meric, I., van der Zande, A. M., Huang, P. Y., Wang, L., Muller, D., Shepard, K. L., and Hone, J. Chemical vapor deposition-derived graphene with electrical performance of exfoliated graphene. *Nano letters*, 12 (6), **2012**, pp. 2751–2756.
- [49] Zhao, L., Rim, K., Zhou, H., He, R., Heinz, T., Pinczuk, A., Flynn, G., and Pasupathy, A. Influence of copper crystal surface on the CVD growth of large area monolayer graphene. *Solid State Communications*, 151 (7), **2011**, pp. 509–513.
- [50] Walter, Andrew L. and Nie, Shu and Bostwick, Aaron and Kim, Keun Su and Moreschini, Luca and Chang, Young Jun and Innocenti, Davide and Horn, Karsten and McCarty, Kevin F. and Rotenberg, E. Electronic structure of graphene on single-crystal copper substrates. *Physical Review B*, 84 (19), **2011**, p. 195443.
- [51] Rasool, H. I., Song, E. B., Mecklenburg, M., Regan, B. C., Wang, K. L., Weiller, B. H., and Gimzewski, J. K. Atomic-scale characterization of graphene grown on copper (100) single crystals. *Journal of the American Chemical Society*, 133 (32), **2011**, pp. 12536–12543.
- [52] Ismach, A., Druzgalski, C., Penwell, S., Schwartzberg, A., Zheng, M., Javey, A., Bokor, J., and Zhang, Y. Direct chemical vapor deposition of graphene on dielectric surfaces. *Nano letters*, 10 (5), **2010**, pp. 1542–1548.
- [53] Tao, L., Lee, J., Chou, H., Holt, M., Ruoff, R. S., and Akinwande, D. Synthesis of high quality monolayer graphene at reduced temperature on hydrogen-enriched evaporated copper (111) films. *ACS nano*, 6 (3), **2012**, pp. 2319–25.
- [54] Reddy, K. M., Gledhill, A. D., Chen, C.-H., Drexler, J. M., and Padture, N. P. High quality, transferrable graphene grown on single crystal Cu(111) thin films on basal-plane sapphire. *Applied Physics Letters*, 98 (11), **2011**, p. 113117.
- [55] Wood, J., Schmucker, S., and Lyons, A. Effects of polycrystalline Cu substrate on graphene growth by chemical vapor deposition. *Nano Letters*, 11, **2011**, pp. 4547–4554.
- [56] Murdock, A. T., Koos, A., Britton, T. B., Houben, L., Batten, T., Zhang, T., Wilkinson, A. J., Dunin-Borkowski, R. E., Lekka, C. E., and Grobert, N. Controlling the orientation, edge geometry, and thickness of chemical vapor deposition graphene. *ACS nano*, 7 (2), **2013**, pp. 1351–1359.

- [57] Meca, E., Lowengrub, J., Kim, H., Mattevi, C., and Shenoy, V. B. Epitaxial graphene growth and shape dynamics on copper: phase-field modeling and experiments. *Nano letters*, 13 (11), **2013**, pp. 5692–5697.
- [58] Yu, Q., Jauregui, L. a., Wu, W., Colby, R., Tian, J., Su, Z., Cao, H., Liu, Z., Pandey, D., Wei, D., Chung, T. F., Peng, P., Guisinger, N. P., Stach, E. a., Bao, J., Pei, S.-S., and Chen, Y. P. Control and characterization of individual grains and grain boundaries in graphene grown by chemical vapour deposition. *Nature materials*, 10 (6), **2011**, pp. 443–449.
- [59] Gan, L. and Luo, Z. Turning off Hydrogen To Realize Seeded Growth of Subcentimeter Single-Crystal Graphene Grains on Copper. *ACS nano*, 7 (10), **2013**, pp. 9480–9488.
- [60] Dhingra, S., Hsu, J.-F., Vlassiounk, I., and D’Urso, B. Chemical vapor deposition of graphene on large-domain ultra-flat copper. *Carbon*, 69, **2014**, pp. 188–193.
- [61] Procházka, P., Mach, J., Bischoff, D., Lišková, Z., Dvořák, P., Vaňatka, M., Simonet, P., Varlet, A., Hemzal, D., Petrenec, M., Kalina, L., Bartošík, M., Ensslin, K., Varga, P., Cechal, J., and Sikola, T. UltrasMOOTH metallic foils for growth of high quality graphene by chemical vapor deposition. *Nanotechnology*, 25 (18), **2014**, p. 185601.
- [62] Liu, W., Li, H., Xu, C., Khatami, Y., and Banerjee, K. Synthesis of high-quality monolayer and bilayer graphene on copper using chemical vapor deposition. *Carbon*, 49 (13), **2011**, pp. 4122–4130.
- [63] Hao, Y., Bharathi, M. S., Wang, L., Liu, Y., Chen, H., Nie, S., Wang, X., Chou, H., Tan, C., Fallahazad, B., Ramanarayan, H., Magnuson, C. W., Tutuc, E., Yakobson, B. I., McCarty, K. F., Zhang, Y.-W., Kim, P., Hone, J., Colombo, L., and Ruoff, R. S. The role of surface oxygen in the growth of large single-crystal graphene on copper. *Science (New York, NY)*, 342 (6159), **2013**, pp. 720–723.
- [64] Bhaviripudi, S., Jia, X., Dresselhaus, M. S., and Kong, J. Role of kinetic factors in chemical vapor deposition synthesis of uniform large area graphene using copper catalyst. *Nano letters*, 10 (10), **2010**, pp. 4128–4133.
- [65] Vlassiounk, I., Regmi, M., Fulvio, P., and Dai, S. Role of hydrogen in chemical vapor deposition growth of large single-crystal graphene. *Acs nano*, 5 (7), **2011**, pp. 6069–6076.
- [66] Choubak, S., Biron, M., Levesque, P. L., Martel, R., and Desjardins, P. No Graphene Etching in Purified Hydrogen. *The Journal of Physical Chemistry Letters*, , **2013**, pp. 1100–1103.
- [67] Tao, L., Lee, J., Li, H., Piner, R. D., Ruoff, R. S., and Akinwande, D. Inductively heated synthesized graphene with record transistor mobility on oxidized silicon substrates at room temperature. *Applied Physics Letters*, 103 (18), **2013**, p. 183115.
- [68] Wang, C., Chen, W., Han, C., Wang, G., Tang, B., Tang, C., Wang, Y., Zou, W., Chen, W., Zhang, X.-A., Qin, S., Chang, S., and Wang, L. Growth of millimeter-size single crystal graphene on cu foils by circumfluence chemical vapor deposition. *Scientific reports*, 4, **2014**.

- [69] Zhang, Y., Zhang, L., Kim, P., Ge, M., Li, Z., and Zhou, C. Vapor trapping growth of single-crystalline graphene flowers: synthesis, morphology, and electronic properties. *Nano letters*, 12 (6), **2012**, pp. 2810–2816.
- [70] Li, X., Magnuson, C. W., Venugopal, A., Tromp, R. M., Hannon, J. B., Vogel, E. M., Colombo, L., and Ruoff, R. S. Large-Area Graphene Single Crystals Grown by Low-Pressure chemical vapor deposition of methane on copper. *Journal of the American Chemical Society*, , **2011**, pp. 2816–2819.
- [71] Chen, S., Ji, H., Chou, H., Li, Q., Li, H., Suk, J. W., Piner, R., Liao, L., Cai, W., and Ruoff, R. S. Millimeter-size single-crystal graphene by suppressing evaporative loss of Cu during low pressure chemical vapor deposition. *Advanced Materials*, 25 (14), **2013**, pp. 2062–2065.
- [72] Kim, H., Song, I., Park, C., Son, M., Hong, M., and Kim, Y. Copper-Vapor-Assisted Chemical Vapor Deposition for High-Quality and Metal-Free Single-Layer Graphene on Amorphous SiO₂ Substrate. *ACS nano*, 7 (8), **2013**, pp. 6575–6582.
- [73] Pirkle, A., Chan, J., Venugopal, A., Hinojos, D., Magnuson, C. W., McDonnell, S., Colombo, L., Vogel, E. M., Ruoff, R. S., and Wallace, R. M. The effect of chemical residues on the physical and electrical properties of chemical vapor deposited graphene transferred to SiO₂. *Applied Physics Letters*, 99 (12), **2011**, p. 122108.
- [74] Lin, Y.-C., Lu, C.-C., Yeh, C.-H., Jin, C., Suenaga, K., and Chiu, P.-W. Graphene annealing: how clean can it be? *Nano letters*, 12 (1), **2012**, pp. 414–419.
- [75] Cheng, Z., Zhou, Q., Wang, C., Li, Q., and Fang, Y. Toward intrinsic graphene surfaces: a systematic study on thermal annealing and wet-chemical treatment of SiO₂-supported graphene devices. *Nano letters*, , **2011**, pp. 767–771.
- [76] Procházka, P. *Preparation of graphene by CVD method. (In Czech)*. Master's thesis, Brno University of Technology, Faculty of Mechanical Engineering, 2012.
- [77] Blake, P., Hill, E. W., Castro Neto, a. H., Novoselov, K. S., Jiang, D., Yang, R., Booth, T. J., and Geim, a. K. Making graphene visible. *Applied Physics Letters*, 91 (6), **2007**, p. 063124.
- [78] MTI Corporation. *Mini CVD Tube Furnace*, 2014. Available online: <http://www.mtixtl.com/MiniCVDTubeFurnace2ChannelGasVacuum-OTF-1200X-S50-2F.aspx>.
- [79] Procházka, P., Bartošík, M., Mach, J., Lišková, Z., David, B., Hulva, J., Konečný, M., and Šikola, T. Shubnikovovy – de Haasovy oscilace na grafenu připraveném metodou CVD. *Jemná Mechanika a Optika*, in press, **2014**.